

**MAGNETIC AND STRUCTURAL STUDIES OF
CORE/SHELL MANGANESE OXIDE NANOPARTICLES
FABRICATED BY INERT GAS CONDENSATION**

by

Mohamed Bah

A thesis submitted to the Faculty of the University of Delaware in partial fulfillment of the requirements for the degree of Masters in Materials Science and Engineering

Summer 2013

© 2013 Mohamed Bah
All Rights Reserved

**MAGNETIC AND STRUCTURAL STUDIES OF
CORE/SHELL MANGANESE OXIDE NANOPARTICLES
FABRICATED BY INERT GAS CONDENSATION**

by

Mohamed Bah

Approved: _____
Syed I. Shah, Ph.D.
Professor in charge of thesis on behalf of the Advisory Committee

Approved: _____
David Martin, Ph.D.
Chair of the Department of Materials Science and Engineering

Approved: _____
Babatunde Ogunnaike, Ph.D.
Dean of the College of Engineering

Approved: _____
James G. Richards, Ph.D.
Vice Provost for Graduate and Professional Education

ACKNOWLEDGMENTS

I would first like to thank my advisor Dr. S. Ismat Shah for providing me with the opportunity and support on this journey. He provided me with all the support and guidance I needed to complete this journey, without which this would not have been possible. I would also like to thank Dr. Feroz Khan, whose tremendous amount of knowledge guided me in understanding complex concept relevant to this project.

I am very thankful to the entire Shah group, who provided a fun, supportive and educational environment around me to allow me to grow as a student and an individual within the group. Their endless support was crucially in my completion of this thesis. A special thanks to Roy Murray for reading and helping with the editing of this thesis. My gratitude is also extend to Dr. Ghulam H. Jaffari, who mentored me in my beginning months of the master program before moving to Pakistan, where he still continues to be a great source of help, through email and Skype.

I am also very thankful to Dr. Ni, Dr. Fei, and Frank for their support on all the microscopy instruments. For all the magnetometry help, and for being a great source of help on general lab issues, I would like to sincerely thank Robert Schmidt of the Physics department.

I will also like to take this moment to recognize all of those who have supported and mentored me throughout the years: Dr. Armando Caro, Dean Michael Vaughan, and Mrs. Marianne Johnson. I would also like to recognize the Greater Philadelphia Region LSAMP Bridge to the Doctorate program for their financial support over the past two years.

Above all, I would like to thank my family for their endless support throughout my education. I dedicate this thesis to them for the sacrifice they made for me throughout the years, and the endless love they keep for me.

TABLE OF CONTENTS

LIST OF FIGURES	v
ABSTRACT.....	vii
Chapter	
1 INTRODUCTION	1
2 BACKGROUND	5
2.1 Manganese Oxide System.....	5
2.2 Exchange Bias.....	9
2.2.1 Theoretical Models	12
2.2.2 Experimental Studies	14
2.3 Magnetism in Nanoparticles	16
3 EXPERIMENTATION.....	20
3.1 Inert Gas Condensation.....	20
3.2 X-ray Diffraction	24
3.3 High Resolution Transmission Electron Microscopy	26
3.4 X-ray Photoelectron Spectroscopy	30
3.5 Physical Property Measurement System.....	35
4 RESULTS AND DISCUSSION	37
5 CONCLUSION.....	47
REFERENCES	49
Appendix	
A SUPPLEMENTAL FIGURE	56

LIST OF FIGURES

Figure 2-1: (A) Crystal Structure of MnO, rocksalt structure, where the oxygen ions are represented by the grey spheres and the white spheres are for the manganese ions. (B) Illustration of the unit cell dimensions of stable manganese oxides. ²⁰	6
Figure 2-2: Schematic illustration of the transformation of manganese oxides under different conditions. ²⁰	7
Figure 2-3: Crystal structure of Mn ₃ O ₄ , spinel structure, where the oxygen ions are represented by the white sphere, the manganese ions on the tetrahedral site, Mn ²⁺ , are represented by the lighter grey spheres, and the manganese ions on the octahedral sites, Mn ³⁺ , are represented by the darker grey spheres. The octahedral sites have 32 atoms per unit cell, while the tetrahedral have 64 per unit cell.	7
Figure 2-4: Crystal structure of MnO ₂ , simple tetragonal rutile structure, where the darker spheres represent the oxygen ions and the lighter spheres represent the manganese ions. ⁴⁷	8
Figure 2-5: Phenomenological model describing the Exchange bias of the hysteresis loop of an FM/AFM bilayer. ^{92, 93}	11
Figure 2-6: Size dependence of coercivity. SD: Single Domain, MD: Mutli-Domain, SPM superparamagnetic, PSD: Pseudo Single Domain. ²¹	19
Figure 3-1: Schematic diagram of the particles growth process. ¹⁰⁰	22
Figure 3-2: Schematic diagram of IGC system with metal pieces feed setup. ⁵³	23
Figure 3-3: Typical basic outlining of a TEM system along with its component. ⁹⁰	29
Figure 3-4: Beam selection for a) bright field image, and b) dark field image.	30
Figure 3-5: Principle of electron emission from an incident X-ray.	32
Figure 3-6: Schematics of XPS analyzer. ²²	33
Figure 4-1: X-ray diffraction pattern of the Mn-O core/shell nanoparticles.	39
Figure 4-2: High resolution transmission electron microscopy image of the Mn-O core shell nanoparticles at different scale: a) 50 nm, b) 20 nm, c) 10 nm, and d) 5nm.	39
Figure 4-3: X-ray photoelectron spectrum of the Mn-O core/shell nanoparticles.....	42

Figure 4-4: FC and ZFC curves of Mn-O core/shell nanoparticles from 5K to 300K with inset from 5k to 72K.	43
Figure 4-5: Hysteresis loops of the Mn-O core/shell nanoparticles from 5K to 42K.....	45
Figure 4-6: Magnetic coercivity of the Mn-O core/shell nanoparticles from 5K to 300K.	46
Figure 4-7: Exchange bias field of the Mn-O nanoparticles from 5K to 300K.	46
Figure A-1: XRD pattern with JCPDS data of MnO, Mn ₂ O ₃ , and Mn ₃ O ₄	56

ABSTRACT

Manganese oxide core/shell nanoparticles were prepared in an inert gas condensation system. X-ray Diffraction (XRD) and High Resolution Transmission Electron Microscopy (HRTEM) studies revealed that the core consisted mainly of MnO which is ferromagnetic (FM) whereas the shell is a mixture of Mn₂O₃ and Mn₃O₄, both ferrimagnetic (FiM), with bulk Curie temperature (T_C) of 39 K and 42 K, respectively. This results in an inverted core/shell structure. Both of these characteristic temperatures were found to be higher than their bulk counterpart, with $T_C = 46\text{K}$ and Néel temperature (T_N) = 150K. A high coercivity field (H_C) of 20 kOe and an exchange bias field (H_{EB}) of 200 Oe were observed from the magnetization measurements performed using a physical property measurement system (PPMS). High saturation magnetization, 10.67 emu/g, persistent magnetic moment above the T_N presumably originating from the short-range spin correlation and other unusual behavior of the exchange bias (EB) and hysteresis loop are observed.

Chapter 1

INTRODUCTION

Manganese oxide (Mn-O) has attracted a great deal of interest over the past few years from both a fundamental and technological point of view. In the presence of water and cations, manganese presents very complex oxide states, even in its bulk form. In addition to its simple oxide states (Mn^{2+} , Mn^{3+} , and Mn^{4+}), many different mixed valence compounds have been discovered¹. This makes manganese oxides very attractive for many applications such as catalysis, electrodes, high-density magnetic storage devices, ion exchangers, sensors, molecular adsorption, in magnetic fluids, biomedical drug delivery, spin valves, ferro-fluid technology, magnetocaloric refrigeration and electronics²⁻¹⁸.

Of these stable oxides the most known are MnO, Mn_2O_3 , and Mn_3O_4 ⁵⁷. Mn_3O_4 is known to be a very good catalyst, where its use has been extended to the combustion of organic compounds at temperatures ranges from 373-773 K^{58,59}. The catalytic properties of Mn_2O_3 are used to assist in the removal of carbon monoxide, and nitrogen oxide from water^{60,61}, as well an oxygen storage components, making it very attractive for use in Li-ion cells⁶².

While bulk MnO is known to be AFM with a T_N of 118K, it shows ferromagnetic behavior as a nanoparticle⁶³. Ortega et.al has shown that the structure of the passivation shell in core/shell MnO nanoparticles depends on the core size being primarily gamma- Mn_2O_3 for small cores and progressively transforming to Mn_3O_4 for larger cores⁶⁷. They have also shown that the core/shell particles exhibit a range of interesting properties such

as large coercivities, EB or enhance anisotropy. Mn_3O_4 has been reported to have a tetragonal structure at room temperature, whereas Mn^{3+} is considered to have a disordered spinel structure⁶⁴. The T_C of both Mn_3O_4 and Mn_2O_3 which are FiM have been reported at or below 43 K^{65, 66, 67}, and another critical temperature was observed at 33K for Mn_3O_4 where the magnetic unit cells become identical^{68, 69}.

The three oxides whose applications are mentioned above are all magnetic. Contrary to similar systems the higher manganese oxides are FiM while the least oxidized are AFM. This is opposite to the system discovered in 1956 by Meiklejohn and Bean where nanoparticles of Co/CoO were made in a core/shell structure, respectively⁷⁴. The T_N in Mn-O system is less than the T_C . The Meiklejohn and Bean system is true for almost all 3d metals except manganese oxide⁶⁵⁻⁷². In this thesis we focus on the magnetic properties of these inverted core/shell ($T_C < T_N$) structures of manganese oxide fabricated by inert gas condensation.

In addition to the curious oxide properties mentioned above that make the nanoparticles of manganese oxide an interesting material to investigate, this inverted core/shell structure further deepens our interest. Core/shell magnetic nanoparticles (NPs) show enhanced magnetization, superparamagnetism, anisotropic in the perpendicular direction. In such a system, the spin-spin coupling of the neighboring atoms keeps the spins parallel or antiparallel⁷³. This coupling does not contribute to the crystal anisotropy, however spin-orbit coupling is the main cause of anisotropy. Since in 3d-transition metal elements the orbital spin is quenched by the crystal field and spins are coupled to the orbital motion of electrons through the lattices, anisotropic energy is required to overcome the coupled pinned state of the electrons.

In multilayer and intermetallic compounds interfacial spin interaction play an important role in tailoring their magnetic and transport properties. Further miniaturizing

leads to other important properties e.g., EB effects between the spins of two different magnetic elements in the neighborhood of each other. This holds their magnetic moments along certain directions even in the absence of a field. In the information storage media, particle size is of great importance, making magnetic systems with EB one of the most investigated fields. Many different models have been developed to understand and explain this phenomenon since its discovery by Meiklejohn and Bean for the Co/CoO fine particles in 1956^{74, 80,80,81,82,88,91}.

The magnetic, electronic, and transport properties of manganese change significantly when the particle size is reduced from bulk to NPs. In recent years these particles have been attracting great interest both in industry and in academia due to the additional dimensionality they offer when engineering new material that exhibit properties different from their bulk counterparts. These differences in properties at nanoscale dimension can be attributed to their large surface to volume ratio. Several phenomena such as lack of saturation, presence of EB, spin flipping, etc., are some of the most attractive properties to be discussed for these materials. The ability to tune these properties makes this an intriguing system to investigate.

In this thesis we focus on the structural, morphological, and magnetic properties, mainly EB effect, of manganese oxide nanoparticles fabricated in an IGC system, and compare the data in relation to similar systems that were fabricated by different methods. Evaporated manganese particles placed in the IGC system in vacuum were passivated through oxygen exposure to create a core/shell structure. The magnetic properties of this system are presented here. The core/shell structure of the samples present an inverse structure from that described by Meiklejohn-Bean⁷⁴, where the T_C of the core, AFM phase, is higher than the T_N of the shell, Ferromagnetic (FM) phase.

The thesis is structured as follows:

Chapter 2 gives a brief background and a literature survey for this system. It gives an account of the stable oxide states of manganese and their bulk magnetic properties, and a brief introduction to H_{EB} phenomenon. In chapter 3 we discuss the experimental setup for the IGC system and the detailed information of the techniques used for the analyses. Chapter 4 is dedicated to the results and discussion of the studied samples. In chapter 5 conclusions are drawn on the success of the fabrication of these NPs using IGC and future work is suggested for the system.

Chapter 2

BACKGROUND

2.1 Manganese Oxide System

The Mn-O system is a very complex one due to the variable valence of manganese cations, Mn^{+2} and Mn^{+3} or Mn^{+4} , and contains four main stable oxides: MnO, Mn_3O_4 , Mn_2O_3 , and MnO_2 , and many other meta-stable mixed states¹⁹. Many of these oxides occur as minerals in nature, i.e. MnO, which is found in nature as a green-colored mineral²⁰. MnO has a rocksalt structure, a cubic structure, with Mn^{2+} and O^{2-} ions at the lattice sites. In fact, all but two, α - Mn_3O_4 and β - MnO_2 , of the stable Mn-O have a cubic structure, shown in Figure 2-1. Mn_3O_4 , known as hausmannite, has a distorted spinel structure at ambient temperature²⁰. Mn_3O_4 structure is $Mn^{2+}[Mn_2^{3+}]O_4^{2-}$, where the tetrahedral and octahedral sites are occupied by Mn^{2+} and Mn^{3+} ions, respectively, as seen in the Figure 2-3²³. The spinel structure of Mn_3O_4 is for the β - Mn_3O_4 , the natural state when it is found in nature as a mineral. This structure can also be fabricated by heating any Mn-O mineral up 1000°C²⁴. Like Mn_3O_4 , Mn_2O_3 also has two stable polymorphs, α - Mn_2O_3 or α -kurnakite and β - Mn_2O_3 or β -kurnakite/bixbyite. β -bixbyite is the naturally occurring mineral. Manganese dioxide (MnO_2) with a simple tetragonal rutile structure^{25,26}, seen in Figure 2-1 have multiple polymorphs. Most of these oxidation states of the Mn-O system have been well documented with the exception of few metastable states²⁷⁻⁴⁰, and their behavior under different conditions is illustrated in Figure 2-2.

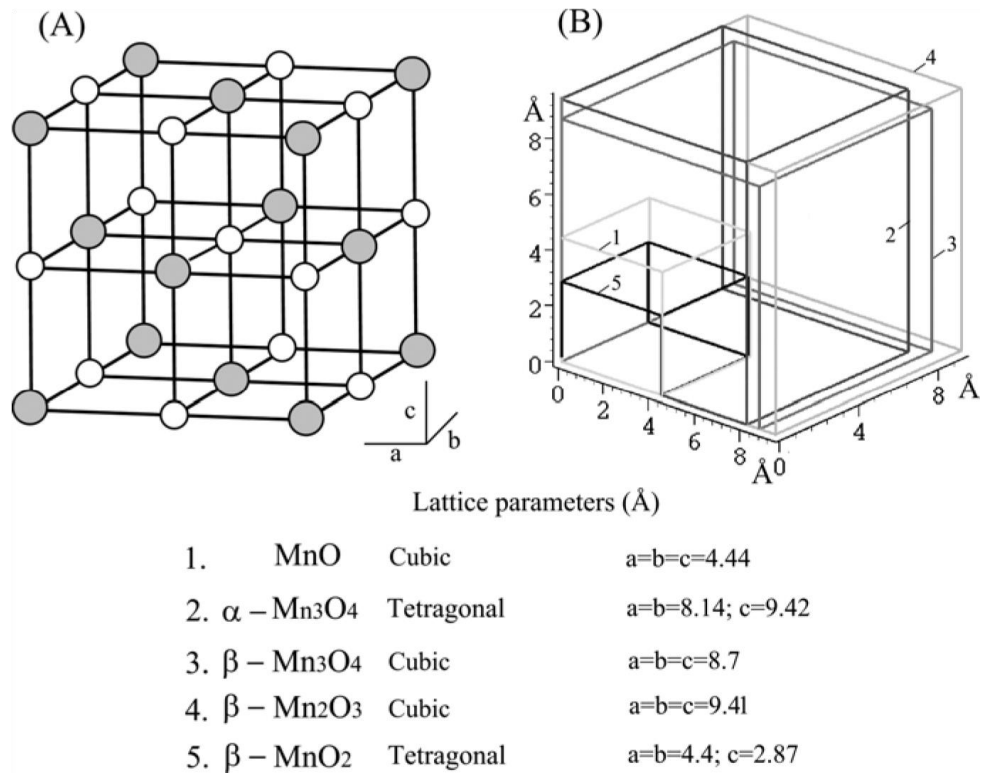


Figure 2-1: (A) Crystal Structure of MnO, rocksalt structure, where the oxygen ions are represented by the grey spheres and the white spheres are for the manganese ions. (B) Illustration of the unit cell dimensions of stable manganese oxides.²⁰

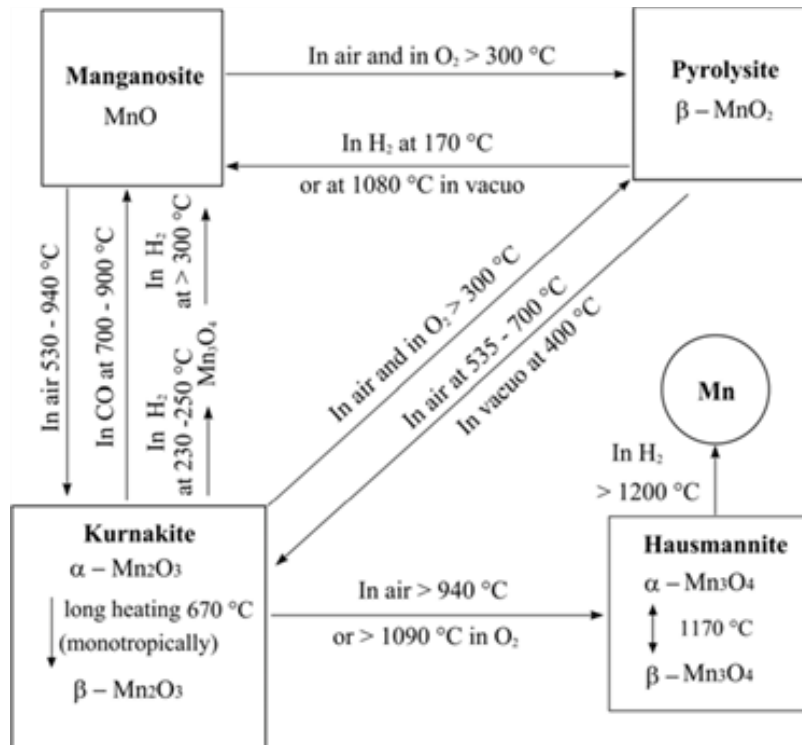


Figure 2-2: Schematic illustration of the transformation of manganese oxides under different conditions.²⁰

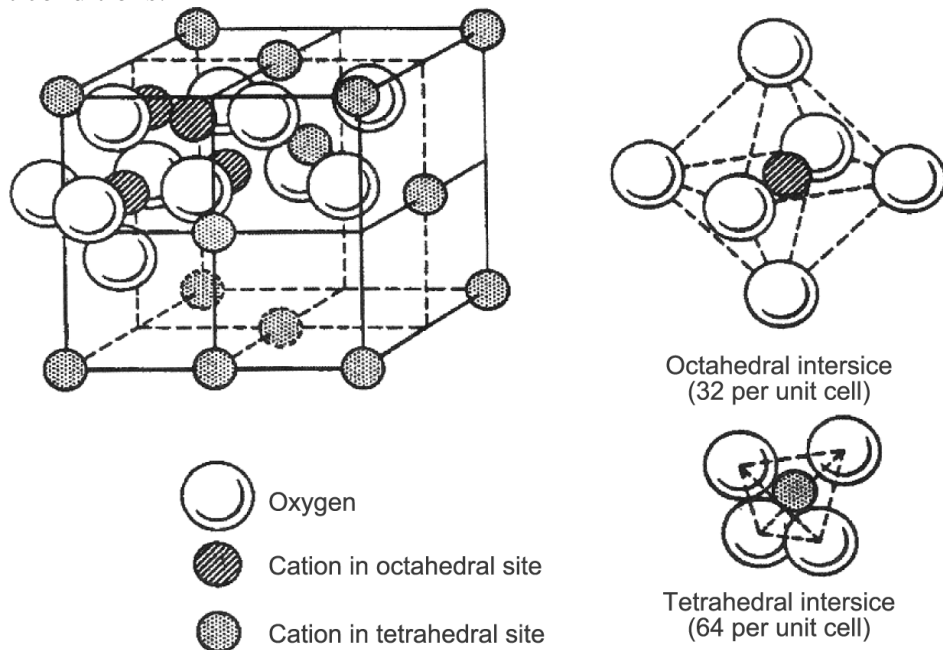


Figure 2-3: Crystal structure of Mn_3O_4 , spinel structure, where the oxygen ions are represented by the white sphere, the manganese ions on the tetrahedral site, Mn^{2+} , are represented by the lighter grey spheres, and the manganese ions on the octahedral sites,

Mn^{3+} , are represented by the darker grey spheres. The octahedral sites have 32 atoms per unit cell, while the tetrahedral have 64 per unit cell.

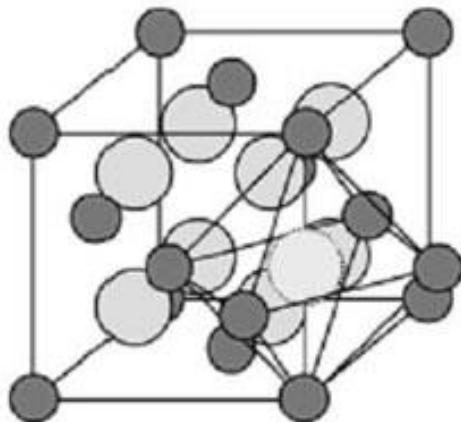


Figure 2-4: Crystal structure of MnO_2 , simple tetragonal rutile structure, where the darker spheres represent the oxygen ions and the lighter spheres represent the manganese ions.⁴⁷

Many different techniques have been utilized to prepare different oxide states of manganese, and recent studies have focused on the preparation of MnO , Mn_2O_3 , and Mn_3O_4 nanoparticles⁴¹⁻⁴⁶. The characterization of these oxides is very difficult due to their lack of well-defined crystallinity and also the mixtures of oxides from most of the preparation methods^{48, 49}. The structures of many of these oxides remain difficult to identify, leaving these oxides with little room to explore with conventional analytical techniques²⁰.

The high surface activity of manganese makes its surface analysis (electron microscopy imaging) a difficult one, even with conventional treatment. Generally used treatments to reduce sample charging can't be employed in the case of manganese since it is sensitive to most surface treatments²⁰. X-ray photoelectron spectroscopy (XPS), which will be discussed in chapter 3, is a commonly used characterization tool in similar materials systems. Although XPS studies of single phases of these oxides are widely available, multiple phase systems with different oxidation states present a difficulty for XPS, even with the aid of software for deconvolution. Manganese ions are at high spin

state, resulting in peak broadening of the Mn 2p doublet due to the multiplet splitting²⁰. The binding energies of the different cations, Mn⁺² and Mn⁺³ or Mn⁺⁴, are only separated by 1 eV. The multitude of the polymorphs of Mn-O with low crystallinity makes it hard to study with X-ray diffraction (XRD, discussed in chapter 3) as well. This is especially true of Mn-O systems prepared with techniques that result in multiple phases.

These difficulties along with the properties of Mn-O are increasingly enhanced as the system size is reduced to the nanoscale, below 100 nm. At this dimension materials exhibit significant behavioral changes in magnetic properties, optical properties, melting points, specific heats, and other properties. The reduction of size results in increased surface activity. This makes metal NPs highly active catalysts, due to the increase of surface atoms, and also explains all the property changes mentioned here. The electrocatalytic activities of Mn-O nanocrystals have shown better electrical and magnetic properties than bulk MnO. Shanmugam and Gedanken¹⁰³ reported that Mn-O-composite electrodes have shown a substantially higher specific activity with a current density of 5.18 mA/cm² which is several orders of magnitude higher than the bulk MnO.

2.2 Exchange Bias

Most important to our discussion here is the effect of these dimensions on the magnetic properties. As mentioned in Chapter 1, these materials have several applications, which exploit the extra degree that these dimensions bring, such as enhancement of magnetization, superparamagnetism, appearance of perpendicular anisotropy and ferromagnetism in nonmagnetic materials. For information storage devices the phenomenon known as EB makes the use of magnetic NPs attractive. Increasing information storage density requires smaller particles, however the decreasing

size results in an anisotropy energy reduction to the point where it becomes comparable to thermal energy. However EB provides an extra anisotropy source.

H_{EB} has been extensively investigated since its discovery by Meiklejohn and Bean for the Co/CoO system in 1956⁷⁴. However, even with the many proposed models^{80, 80, 81, 82, 88, 91}, the true nature of H_{EB} is still not well understood. It has been a common understanding that an observed shift in the hysteresis loops exists for many metal/metal oxides that have been cooled from a temperature above the T_N to a temperature below the T_C . The shift is then attributed to the interaction between the coupling at the interface of the FM and AFM. To simply illustrate this, Meiklejohn first developed a model based on a thin film bilayer. Before discussing this model, we will first present a magnetic interaction model of the interface of such a system. The figure below shows the different steps observed at the interface of FM/AFM.

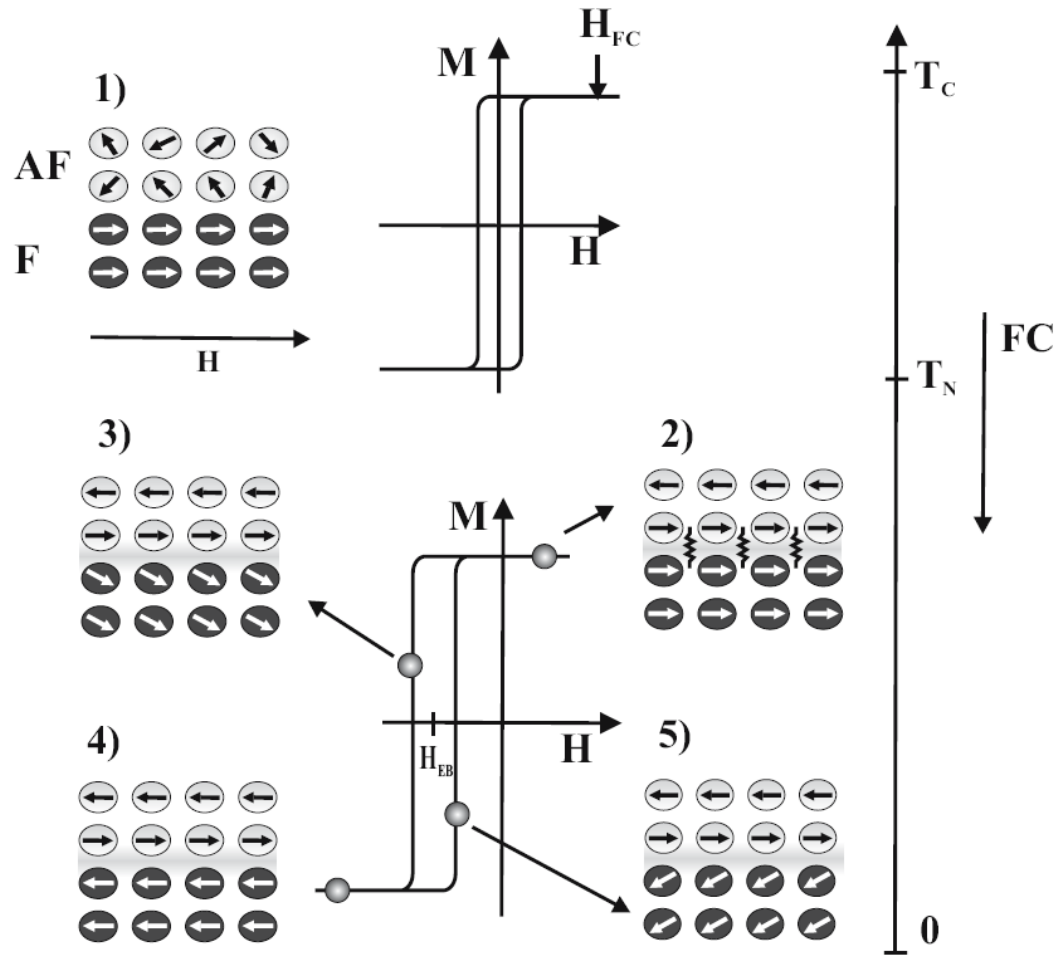


Figure 2-5: Phenomenological model describing the Exchange bias of the hysteresis loop of an FM/AFM bilayer.^{92, 93}

In the schematic representation of a bilayer film above, where the bottom films are AFM and FM, the interaction of the spins on the individual films are shown and their correlation to the shift of the hysteresis loop also depicted from the above to the bottom loop. In the first loop, it is shown that around the T_C , the loop is well centered/symmetric. Around this temperature, the AFM does not affect the magnetic response of the FM loop, Figure 2-5-1). When the bilayer film is cooled below its T_N with an applied field, the spins get aligned with the applied field. The spins from the AFM remain unchanged as the field is swept. However those of the FM rotate opposite of the direction of the sweeping field. While these spins are rotating, they experience a

torque from the pinned spins of the AFM layer if the anisotropy constant of the AFM is large enough, Figure 2-5-2). To overcome this force, a larger field is needed. This large applied field is known as the coercivity field (FC). At higher field the spins are reversed due to their unidirectional anisotropy, Figure 2-5-3). This anisotropy, along with microscopic torque exerted on the FM layer by the AFM layer at the interface, help quickly reverse the spins orientation when a small change in field is applied in the opposite direction, resulting in a smaller coercivity field, Figure 2-5-3) and 5), therefore shifting the symmetry of the loop in the direction opposite of the positive field.

Therefore this shift, H_{EB} , can be mathematically calculated from the difference of the coercivity in the negative and positive direction, $H_{EB} = \frac{H_{C^-} - H_{C^+}}{2}$ where H_{C^-} is the coercivity field needed in the negative field direction to overcome the microscopic torque, while the H_{C^+} is the coercivity in the positive direction. Again this illustration is a simple model to help with the visualization of the shift in a bilayer AFM/FM system. It does not however explain the interface structure of the system, the interface magnetic coupling direction, cooling field intensity dependence, coercivity (H_C), nor the enhancement of the shift.

2.2.1 Theoretical Models

In the model proposed by Meiklejohn for a bilayer AFM/FM system, he calculated the rotational hysteresis, energy, and loss at the interface of a bilayer system with a single domain AFM weakly coupled with a single domain FM at the interface. From the energy model that he proposed for the interface, by using a vector model, and the assumption that anisotropy constant of the AFM is must greater than of the FM, H_{EB} was given as follows.

$$H_{EB} = \frac{J_{F/AF}}{a^2 M_F t_F} \quad (2.1)$$

where $J_{F/AF}$ is the interfacial exchange constant, a the lattice parameter, M_F the FM saturation magnetization, and t_F the thickness of FM layer. Due to the assumption mentioned above and lack of consideration of the important structural parameters, the shift calculated by eq. 2.1 is several orders of magnitude different from observed experimental values. This model also only considers the simplicity of the geometry of thin films.

Other models have since been proposed to address some of the issues that are evident in the proposed model of Meiklejohn. A model proposed by Nèel removed the assumption made by Meiklejohn, where he considered a system that has a weakly anisotropic uncompensated AFM interface layer which is ferromagnetically coupled to a FM layer⁸¹. In 1987, Malozemoff proposed a model that was significantly better at estimating the H_{EB} . His model decreased the H_{EB} by a factor of $2a / \sqrt{(A / K)}$, eq. 2.2, where K is the anisotropy constant. In his model, he assumed a system where the EB mechanism is a response to randomness in the exchange interactions⁸².

$$H_{EB} = \frac{2\sqrt{A_{AF}K_{AF}}}{M_F t_F} \quad (2.2)$$

where A_{AF} is the exchange stiffness of the AFM layer. Although this model is a better approximation than the two listed so far, it has its limits as well, since it only considers defect free systems which are not ideal for any practical system.

Mauri et al also proposed a model of the H_{EB} where the system only allows an infinitely thick AFM layer, thicker than the width of the domain wall; however it

restricts the size of the FM layer, to a single domain size⁷⁵. The model has been successful in predicting the H_{EB} of FM/AFM systems such as Ni/NiO and Co/CoO systems. The system still fails to explain other system such as EB that requires AFM coupling of the interface spins⁷⁷, including systems where large H_{EB} are observed in the compensated interfaces rather than the uncompensated ones.

Recent theories have developed to more closely correlate with observed experimental data. Kiwi et al. used a model that considered unfavorable domain walls and large anisotropy constant of the AFM layer (K_{AFM}). This introduced the idea of frozen interfaces, where the first layer of the AFM layer freezes into displaced spins (canted spins) configuration^{78,79}. Nowak et al. proposed the Domain State (DS) model for EB²¹. In their model, they diluted the AFM region with nonmagnetic atoms or defects. With this model they proposed that the formation of defects in the AFM region creates domain states in the AFM causing domain wall formation through the defect thereby reducing the energy needed to form the wall. This led to their conclusion that the H_{EB} originates in the domain state in the volume of the AFM⁸⁰. Just as in the Kiwi model, they were able to obtain consistent results data agreed with experimental values.

2.2.2 Experimental Studies

As mentioned above, experiments were conducted and compared to theoretical models. These experiments have also helped set some understanding on this phenomenon, H_{EB} . Apart from the experiments conducted by Nowak et al., other experiments have also been conducted to support the model. In these experiments, i.e. creation of defects in Co/CoO system by introduction of nonmagnetic Mg or by over oxidation of the AFM layer⁷⁶, it was found that domain

formation in the AFM layer led to the enhancement of the H_{EB} by a factor of 3 or 4. These experiments show vertical shift of the hysteresis loop which in turn confirmed excess magnetization. The vertical shift of the hysteresis loop can either be upward or downward from the magnetization axis, depending on whether the spins are FM or AFM. This was first observed in FeF_2/Fe and MnF_2/Fe systems by Noguès et al.⁷⁷. The direction of the shift has been attributed to the structure of the layer in small cooling fields (H_{cf}), although always upwards in the case for large H_{cf} ²¹. From this understanding, it was then clear that there exist a correlation between positive H_{EB} and the nature of the FM/AFM coupling. It was observed that a downward shift can be attributed to the antiferromagnetic coupling of the FM/AFM interface; however an upward shift corresponded to the ferromagnetic coupling of FM/AFM interface, where a negative H_{EB} is observed.

All the mentioned theories and experiment worked in the regime where FM layer is thick enough. It is important to note that a lower limit of the FM layer thickness, t_f , is also important. Too thin of a FM layer may lead to broken continuity in the layer, therefore leading to no H_{EB} , rendering the discussion of this anisotropy useless. The lower limit of this layer depends on the material being investigated, but is usually in the range of few nm. It has also been observed that further increase in DS in the AFM layer may reduce H_{EB} , since the increase of DS suppresses the AFM order²¹.

The temperature range for H_{EB} observation was said to be $T_N < T < T_C$, however many studies have shown the shift to persist at a temperature below the T_N ⁸³⁻⁸⁷. Many studies have actually shown that the H_{EB} is zero at a temperature referred to a blocking temperature (T_B)^{86, 87}. T_B has been referred to as the

temperature at which the blocked spins enters a superparamagnetic state, and is defined as follows:

$$T_B = \frac{\Delta E}{k_B \ln(v_0/v)} \quad (2.3)$$

where ΔE is the energy barrier, k_B the Boltzmann constant, v_0 the attempt frequency and v the measured frequency.

T_B has been shown to vary with the size of the AFM layer, with the T_B of layers less than 10 nm known to be less than those of the bulk oxides. However observation of the $\text{Fe}_3\text{O}_4/\text{CoO}$ system have also indicated increase in T_B , where the thickness of the AFM layer is less than 5 nm, compared to the bulk. In this system the increase in T_B was attributed to the proximity to the Fe_3O_4 high T_C , suggesting that the AFM ordering in this system is initiated in the Fe_3O_4 layer.

2.3 Magnetism in Nanoparticles

All of the discussed models and their supportive experiments so far have only consider the thin film system. However, recent developments on nanoparticle preparation techniques have led many to investigate the original observation made by Meiklejohn in 1956⁹⁴⁻⁹⁷. Size reduction in nanoparticles makes their investigation an appealing one, as it brings novel features such as superparamagnetism²¹. This size reduction has a limit when it comes to magnetic studies. As the magnetic particles can only support one domain they have a size limit. Single domains are formed because of the energy minimization by the competition of the magnetostatic energy and the domain wall formation energy. For a magnetic system to minimize its energy, it divides into magnetic domains, at least two. The resulting domains in turn form walls between each

other to reduce the exchange energy between spins. The optimization of these two energies limits the size at which a system can be reduced. The size of a single domain (ds) is approximated by the ratio of the domain wall energy per unit area over the square of the saturation magnetization, if one ignores the proportionality constant. Decreasing the system size also decreases the anisotropy energy, KV of the system, where V is the system volume.

In such a system, the energy can be explained by the Stoner-Wohlfarth model, eq. 2.4, which is the simple model that explains magnetism in single domain, and non-interacting magnetic nanoparticles based on coherent magnetization reversal²²,

$$E = KV\sin^2\theta + HM_S \cos(\theta - \phi) \quad (2.4)$$

where H is applied magnetic field, M_S is the saturation magnetization, θ is the angle between magnetization angle and the easy axis, and ϕ is the angle between the applied field and the easy axis. Therefore as the system volume, V , decreases the energy of the system becomes free to respond to applied fields. In response to the applied field, the free magnetic moments align themselves with the field, $\mu_p = M_S V$. At such dimensions thermal effects, $k_B T$, also disturb the alignment of the spins. And for systems with small anisotropy constants, the behavior is similar to that of a paramagnetic system with saturation, also known as superparamagnetism (SPM). In SPM the freed spins of the individual particles are in the direction of the easy axis when there's no field present. This preferred orientation of the spins creates an energy barrier (E_a), which has to be met to prevent magnetization reversal. SPM becomes a time dependent phenomenon, which takes into account thermal energy.

The time it takes for a system magnetization to be reversed is called the relaxation time (τ) and is proportional to the Boltzmann constant, eq. 2.5.

$$\tau = \tau_0 \exp\left(-\frac{KV}{k_B T}\right) \quad (2.5)$$

where τ_0 is the attempt timescale and is in the order of 10-12 sec, and T is the temperature in Kelvin. Here, at SPM, KV is similar to the Ea and becomes comparable to $k_B T$. From eq. 2.5, it is evident that experimental time plays a big role when investigating systems close to their SPM state, and also that it is temperature dependent. Therefore the temperature at which a given system volume switches from a stable ferromagnetism to SPM is called T_B . This temperature is also affected by the applied field. Therefore the HC of different particle size can be determined around the critical point of the system. This field is given by eq. 2.6.

$$H_C = \frac{2K}{M_S} \left(1 - \frac{25kT}{KV}\right)^{1/2} \quad (2.6)$$

And is also shown in **Error! Reference source not found.** where it is evident that the C is highest in the single domain region. In the single domain region, magnetic reversal is attained by the rotation of the entire spin structure, in a coherent nature. However, incoherent motion can also aid in the rotation of the spins²¹.

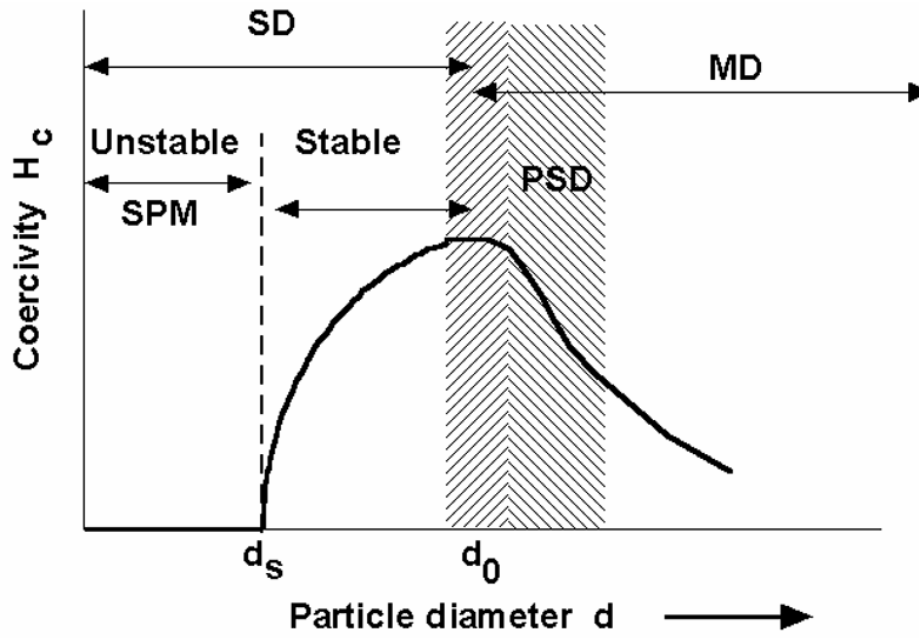


Figure 2-6: Size dependence of coercivity. SD: Single Domain, MD: Mutli-Domain, SPM superparamagnetic, PSD: Pseudo Single Domain.²¹

Chapter 3

EXPERIMENTATION

Several techniques have been developed to prepare NPs over the years due to their potential applications^{70, 71, 72}. Traditional fabrication techniques, such as chemical routes, are at a disadvantage due to wider range of particle size distribution and the need for surfactants to stabilize the particles to prevent agglomeration, which can lead to adverse physical properties⁷⁰. However gas condensation techniques such as inert gas condensation (IGC) have the ability to produce particles with a narrow particle size distribution^{70, 71}. This control is made easy by tuning four parameters of the fabrication system: chamber temperature, chamber pressure, proper selection of inert gas, and inert gas circulation rate. In this chapter the synthesis of core/shell manganese oxide and its characterization are discussed. The samples studied in this thesis were prepared by an IGC system. XRD, HRTEM, and XPS were used for the characterization of the samples, while magnetic measurements were done in the PPMS.

3.1 Inert Gas Condensation

Inert Gas Condensation (IGC) is a system in which metallic vapors are rapidly cooled into solid phase by a condenser gas, i.e. Helium. This process was first used by Pfund et al. in 1930, when they synthesized bismuth nanoparticles by evaporating bulk bismuth from tungsten wire⁵⁰. Since then many metallic nanoparticles have been synthesized by IGC, a system refined by Gleiter's group⁴⁹. Methods of loading the metal into the evaporating system vary from wire feed to a direct placement of pellets on the boat or crucible. In this thesis, bulk metals are placed in an alumina coated tungsten boat or crucible and resistively heated by a power source until they evaporate.

The IGC chamber was evacuated by a mechanical pump followed by high vacuum pumping with a turbo-molecular pump to achieve a vacuum of approximately 2×10^{-6} Torr over a period of 24 hours. The samples were then heated by slowly ramping up the source power until they melt and create a whitish glow. The temperature of the molten samples was recorded using an infrared gun pointed at the glowing samples. When heated to approximately 1200°C, the samples begin to evaporate into metallic vapors which are quickly swept away from the heating source by circulating helium gas through a Roots blower. Due to the high thermal conductivity of the helium carrier gas, the metallic vapors were cooled quickly as they were swept through the chamber. The interaction between the manganese vapors and the molecules of the inert gas drove this decrease in temperature. During the cooling process, the metallic vapors supersaturate the carrier gas causing the onset of nucleation. The nuclei further agglomerate before being collected on the porous filter located in the system.

In the fabrication process, the inert gas pressure, cooling rate, and evaporation temperature are carefully tuned to control the particle size. Of these parameters, pressure is shown to have the largest effect on particle size. Although diffusion is the main transport medium of these metallic vapors, it is the partial pressure of inert gas that contributes the most in controlling the particle size^{53,54}. Increase in vapor pressure during the growth periods yield large particles. The higher pressure allows more nuclei to coalesce. Increase in temperature also results in an increase in the size of the particles. Higher temperature results in higher kinetic energy therefore higher activity from the particle. Higher activity leads to an increase in probability for coalescence of the particles⁵⁵. Thermal conductivity also plays a role in controlling the size of the particles, since it has been shown that temperature affects the particle size. Helium has been

chosen as the inert gas of interest here, since it has the highest thermal conductivity and among the inert gases.

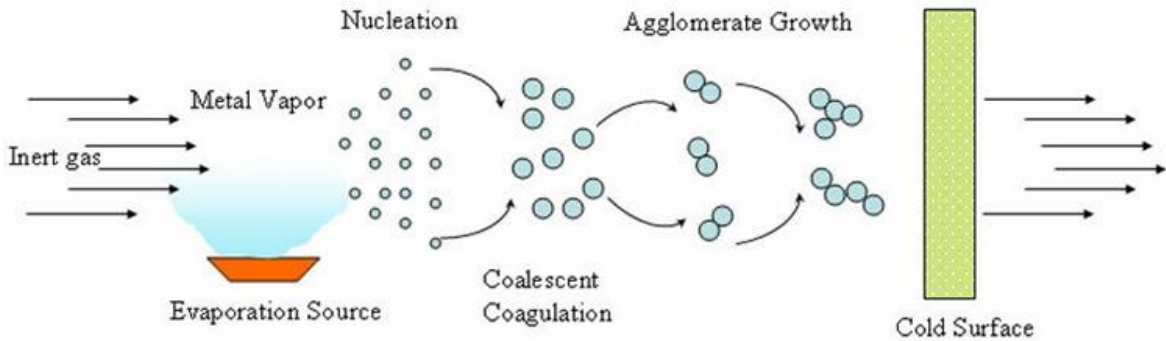


Figure 3-1: Schematic diagram of the particles growth process.¹⁰⁰

Figure 3-1 shows the three stages of particle growth in an IGC system. The first is the nucleation stage. In this stage onset of nucleation takes place when the metallic vapor super saturate due to the decrease in temperature as the vapor is swept away from the heating source by the helium gas. The increase in the vapor pressure as the number of nuclei increases results in further coalescence of the metallic vapors, further down the chamber. This is the second stage in the growth process. Here the nuclei coagulate and form bigger particles. The increase in size of the particle increases the probability of their collision, which further increases size before they are collected on the cold surface of the porous filter.

The IGC system used for the samples preparation is shown below with a slight modification to the conventional system in our lab to accommodate evaporation from metallic pieces. The main components of the system are displayed. The alumina coated tungsten boat filled with Mn pieces was resistively heated with a high current supply. In our initial run of the system the pieces were flying off the boat as the power for the heating source was increased. Therefore, a molybdenum sieved sheet with pore size

around 1 mm was placed on top of the boat to keep the pellets from flying off before they were completely melted. A Roots blower circulates helium through the system, forcing particles into the filter. M. B. Ward had previously employed a similar setup to evaporate manganese (Mn) pieces⁵⁶.

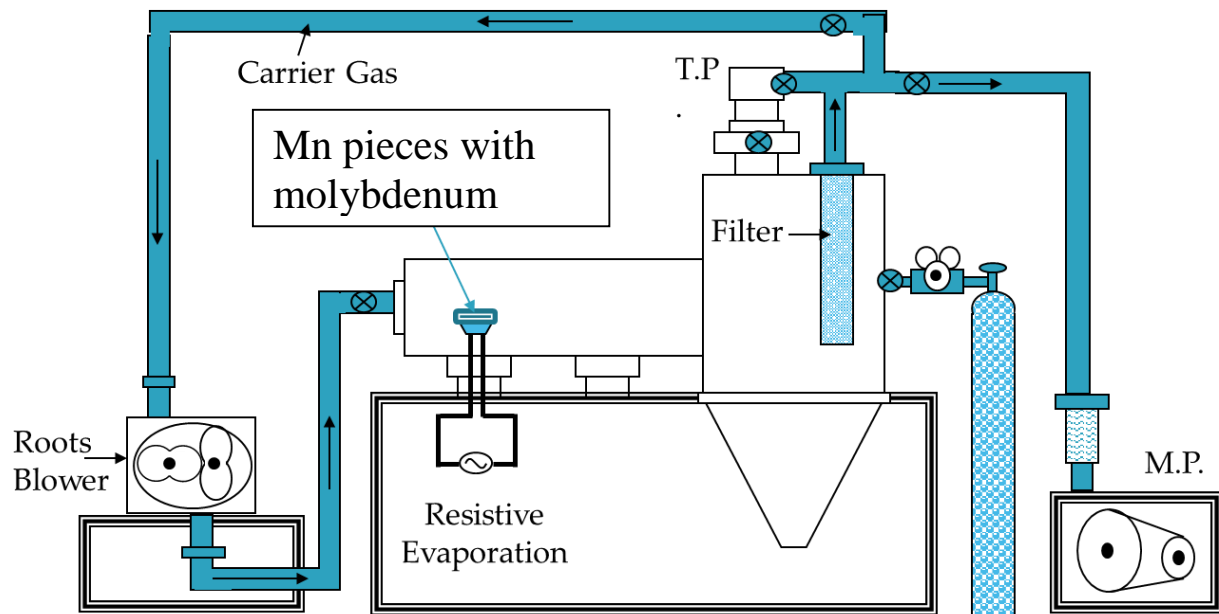


Figure 3-2: Schematic diagram of IGC system with metal pieces feed setup.⁵³

All of the pellets placed onto the boat evaporated quickly when the temperature of the boat reached the melting point of Mn. This results in an abrupt increase of the partial pressure above the alumina boat. This limits the size control that exists with a system where a wire feeds above the heating source. This also leads to lower yield of particles collected on the surface of the porous filter. Most of the particles are lost to the surrounding walls near the heating source.

Before sample preparation, the chamber was evacuated to high vacuum (HV). After the pieces were inside the alumina boat, the system was evacuated, first to low vacuum, in the order of 10^{-3} Torr, by a mechanical pump (M. P.), then to high vacuum, 2×10^{-6} Torr, by a turbo-molecular pump (T.P.). HV is necessary in IGC before filling the

chamber with helium to a desired pressure. This helps increase the partial pressure of helium which is the driving force in super cooling the molten vapor, since it has a very high thermal conductivity. The M.P. also helps keep the desired gas pressure inside the system remain constant during growth. Thermocouple and cold cathode gauges were used in reading the pressure inside the chamber. A vent located at the bottom of the cone helps bring the system to atmospheric pressure for passivation once growth of the nanoparticles is completed. The helium cylinder at the left of the M.P. is used to provide helium inside the chamber to reach a desired pressure. For the samples investigated here, the system was maintained at 500 mTorr pressure throughout the growth. The particles were exposed to air for about 3 hours by opening the vent valve. The passivated particles were then collected by scraping the wall of the filter.

3.2 X-ray Diffraction

X-ray diffraction (XRD) technique is employed in this thesis to determine the crystal structure of the prepared samples. This technique uses X-rays with a wavelength comparable to atomic dimensions. The dimension of these X-rays permits the investigation of the interatomic distances in the prepared samples. The technique helps with identification of phase, lattice constant, crystal size, texturing, etc. In 1912, in a study conducted by Bragg, X-rays were used to determine crystal structure by observing diffraction patterns. Bragg derived eq. 3.1 to explain the generation of diffraction pattern in a sample under X-rays bombardment.

$$n\lambda = 2d\sin\theta_{hkl} \quad (3.1)$$

In eq. 3.1, known as Bragg's law, Bragg showed that when a monochromatic X-ray beam of wavelength, λ , is incident on a crystalline material at an angle, θ , diffraction patterns are observed when there's constructive interference of the various planes in the crystalline sample. The distance between these planes is known as the d-spacing, and represented by d in eq. 3.1. According to Bragg's equation, the patterns are formed when the distance traveled by the X-rays reflected from successive planes differs by a whole number, n , of wavelengths. The $(h k l)$ in eq. 3.1 refer to the miller indices, a notation method employed in crystallography to identify planes in crystal lattices.

In a given sample, where the distance between the crystal plane differences are set, one can determine the range of the d-spacing that can satisfy the Bragg's law by varying the θ between the incident X-ray beam and the sample. This data can provide other characteristics of the sample, not only limited to phase identification such as lattice constant, crystal size, etc. At such limits, peak broadening has been observed. Scherer used this broadening to help determine the average particle size by deriving eq. 3.2.

$$D = \frac{0.9\lambda}{\beta \cos\theta} \quad (3.2)$$

where D is the mean particle size, and β the full width at half maximum (FWHM) of the peak in radians. For most instruments have their own errors that contribute to measured FWHM (β_0), this has to be correct for each instrument before the application of eq. 3.2 can be used to determine D .

It is important to note that strain beside particle size reduction can affect peak broadening; however FWHM from the instrument noise does not. Therefore the total broadening, β , shown in eq. 3.2 can be described by the following equation,

$$\beta_t^2 \approx \left[\frac{0.9\lambda}{D \cos\theta} \right]^2 + (4\varepsilon \tan\theta)^2 + \beta_0^2 \quad (3.3)$$

where ε is the strain. Eq. 3.3, does not, however, take into consideration the spectral broadening, which has been observed to be dominant at $2\theta > 50^\circ$ ⁸⁹.

In this thesis a monochromatic Cu K α radiation (λ (K α_1) = 0.15406 nm) is utilized since this wavelength is in the same range as the features of interest. The angle between the incident X-ray beam and the samples were varied from 30° to 90° with a constant scan rate of 1.2°/min and a step size of 0.02°.

3.3 High Resolution Transmission Electron Microscopy

High resolution transmission electron microscopy (HRTEM) is utilized to explore the structure of the NPs. It is imperative to know the true structure of the samples in order to make a good interpretation of the results from other analyses. In the case of the magnetic materials, a correlation between magnetic behavior, particle agglomeration and morphology needs to be understood. It helps identify polymorph structures that might be shown on XRD as simple amorphous material, or further show amorphous material that might be masked by crystalline phases. This is especially important for core/shell nanoparticles where the core and shell will have different crystalline phases.

Transmission electron microscope (TEM) allows the observation of materials in micro and submicron ranges. This microscope operates like a light microscope; however it uses electrons instead of light. The smaller wavelength produced by the electrons compared to that of light makes it possible to get a higher resolution (R), in the order of thousands better, than that of light microscopy, making the TEM very attractive for probing small length scales. This resolution is shown by eq. 3.4. Resolution is usually denoted as d however here we use R to avoid confusion since d has already been assigned to the distance between crystal plans.

$$R = \frac{0.61\lambda_e}{\mu \sin\varphi} \quad (3.4)$$

Where μ is the refractive index of the viewing medium and is usually approximated to be 1, φ the semi-angle of collection of the magnifying lens, which is only a few degrees, and λ_e the wavelength of the electron beam, not to be confused with the λ given above for the wavelength of the X-ray source. In TEM the accelerating voltage (V) range from 100 kV and 400 kV, and is related to λ_e by,

$$\lambda_e \approx \frac{h}{\sqrt{2m_0E \left(1 + \frac{E}{2m_0c^2}\right)}} \approx \frac{1.22}{\sqrt{V}} \quad (3.5)$$

where h is the Planck's constant, E the energy of the accelerated voltage, m_0 the rest mass of an electron, and c the speed of light.

In TEM, an electron beam with λ_e emitted from a filament or field electron is directed to a thin specimen by a set of condenser lens. A schematic description of a typical TEM is given in Figure 3-3, along with its components. A typical TEM has a condenser system, objective lenses, diffraction/intermediate lenses, projective lenses, an image observation screen, and a vacuum system. Two condenser lenses are used to condense the electron beam. The objective, intermediate and projector lens are used to focus an image or the diffraction of specimen on the screen; the objective lens is probably the most important lens since it generates the first intermediate image. Different modes of imaging are utilized to obtain an image of interest from the numerous signals produced from the interaction of the directed beam and the sample. The interaction of this directed and focused beam with the sample result in elastic and inelastic scattering of the electron beam. The general signals are backscattered electrons and secondary electrons. The different modes of imaging available to TEM use these electrons to do elemental

analyses, topographical imaging, and compositional analyses. From the scattered electrons an image is formed by inserting an aperture into the back focal plane of the objective lens, thereby blocking most of the diffracted pattern except those of interest. When the directly reflected beam is chosen, the image is said to a bright field (BF) image, whereas the image is said to dark field when any other scattered electrons are used to form the image. Generally, the electron diffraction pattern will be obtained first. A bright field (BF) image is obtained by selecting the center beam to form the image. A dark field (DF) image is obtained by collecting any other scattered electrons of the beam to provide the image.

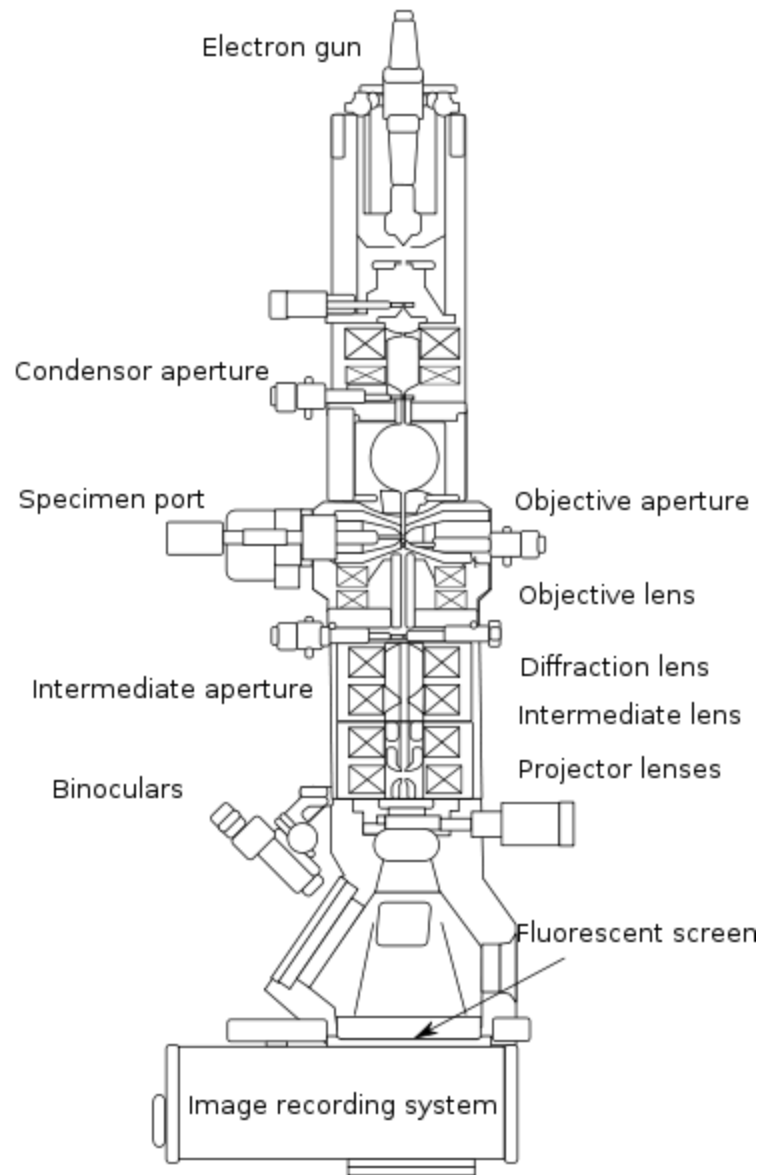


Figure 3-3: Typical basic outlining of a TEM system along with its component.⁹⁰

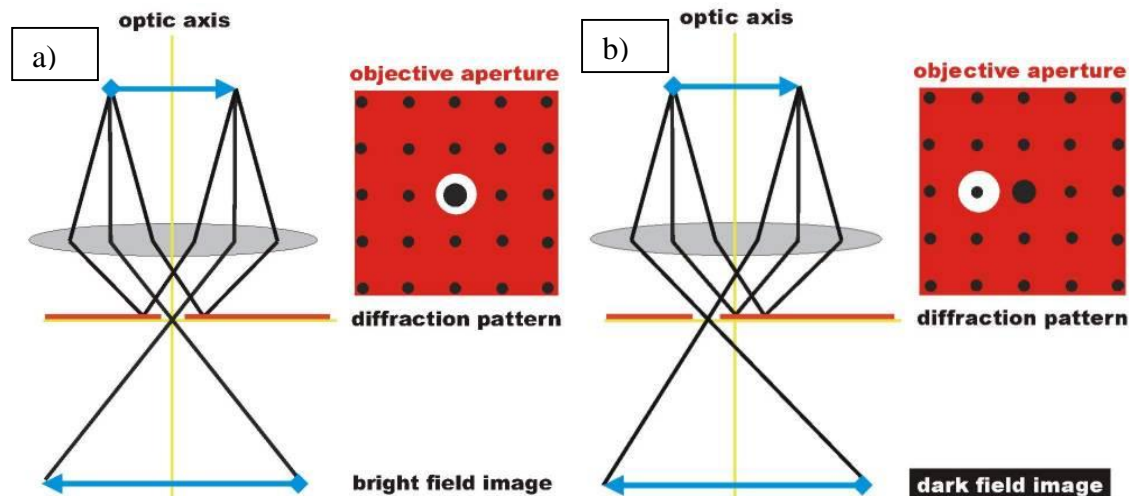


Figure 3-4: Beam selection for a) bright field image, and b) dark field image.

The JEOL 2010FX TEM was used to study the morphology of the samples. In this system an accelerating voltage of 200 kV was used to create an electron emission field beam. This beam was focused onto the samples through focusing apertures, metal apertures and magnetic lenses. The interaction of this directed and focused beam with the samples result in elastic and inelastic scattering of the electron beam. The interactions result in backscattered electrons and secondary electrons. These electrons can be used to do elemental analyses, topographical imaging, etc. This system is used here to shed light on the morphology of the samples, core/shell composition, and the particle size range. It also helped determine that the samples were highly polymorphic.

3.4 X-ray Photoelectron Spectroscopy

X-ray photoelectron spectroscopy (XPS), with an Al K α source (1487 eV), is utilized to investigate the binding energies of the electrons of the prepared samples. XPS has become a very popular technique in recent years. The technique has been well developed since Siegbahn et al. first used photoelectron spectroscopy in the 1950s as a viable tool to investigate electronic structure¹⁰². Photoelectron spectroscopy is a

technique that utilizes a beam of photons with energy $h\nu$ to irradiate a sample. Electrons produced, photoelectrons, from the interaction are then ejected into a vacuum system to be analyzed. This process is called photoemission, and the energy, $h\nu$, of the photoelectrons was first predicted by Einstein theory of photoemission to be,

$$K.E. = h\nu - E_B \quad (3.6)$$

The eq. 3.6 states that the kinetic energy (K.E.) of an ejected photoelectron is the difference of the incident beam and the binding energy of the electron in the k^{th} orbital of the specimen.

This information is collected and analyzed by an electron energy analyzer or detector. The resulting spectrum is a graph where the intensity of the photoelectron, the electron count per second, is plotted against their E_B . All XPS spectra show varying shape peaks, which correspond to the transition of the different core electrons levels of the samples, i.e, for 2p, 3s, and 3p and electrons. These peaks are due to electrons that escape the sample without any inelastic collisions with other atoms¹⁰². However other interactions of the electrons do take place, thereby reducing the energy of the electron, this is observed as the background on the high binding energy side of the peaks. Therefore, it can be seen that this technique can have many complications and a clear understanding or modeling of this background or of binding energy at low energies can be problematic.

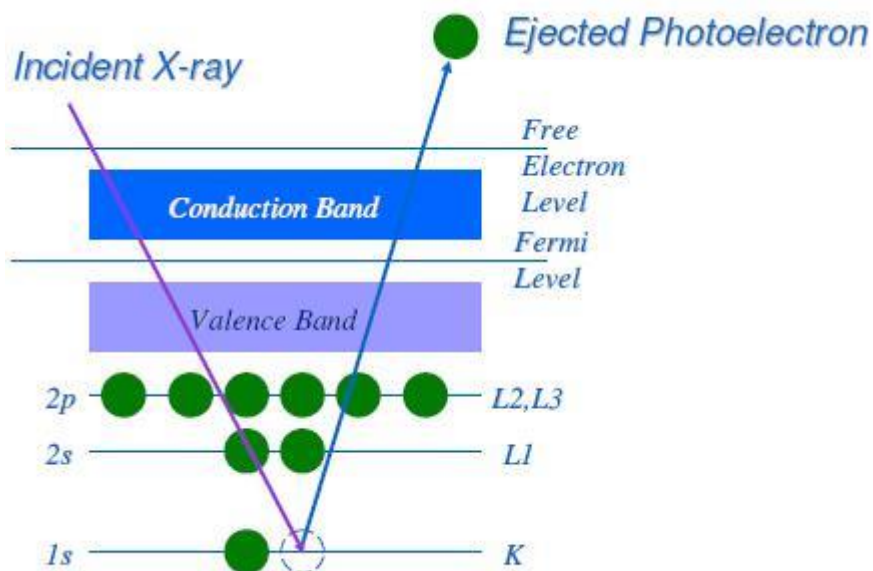


Figure 3-5: Principle of electron emission from an incident X-ray.

It has been observed that resulting peaks in the spectrum are related to the density of the electronic states. Electronic states in metals and semimetals are quantized and consist of discrete bands. Therefore, this technique can be used to determine kinetic energy distribution in metals and semiconductors. However other phenomenon, such as plasmon losses, multiplet splitting, and other satellite peaks add different degree of difficulty in the analysis of the spectra.

A typical XPS system has the following main components:

- *An X-ray source* usually an X-ray tube, monochromators or synchrotron sources are also used. Monochromators are used to improve resolution of the incident beam from X-ray tubes, while synchrotron sources provide very high intensity X-ray beams.
- *An ultra-high vacuum chamber* where the emitted electron is allowed to reach a detector without being subject to collision with gas molecules that may contaminate the surface of the sample¹⁰².

- *An electron energy analysis and detection usually a hemispherical analyzer with two concentric hemispheres and an electrostatic lens system. Here, electrons are accelerated around a curve by a constant applied voltage, from the inner and outer spheres of the analyzer, in order to filter electrons that have high energy to pass through the system and reach the collector plate. This helps reduce the signal to noise ratio, therefore increasing the resolution of the collected spectrum. The down fall of this system is the loss of sensitivity by reduction of slower moving electrons, even with the employment of focusing lenses. This lens system helps adjust the spatial and angular resolution of the analyzer; helps reduce the loss of slower moving electron.*

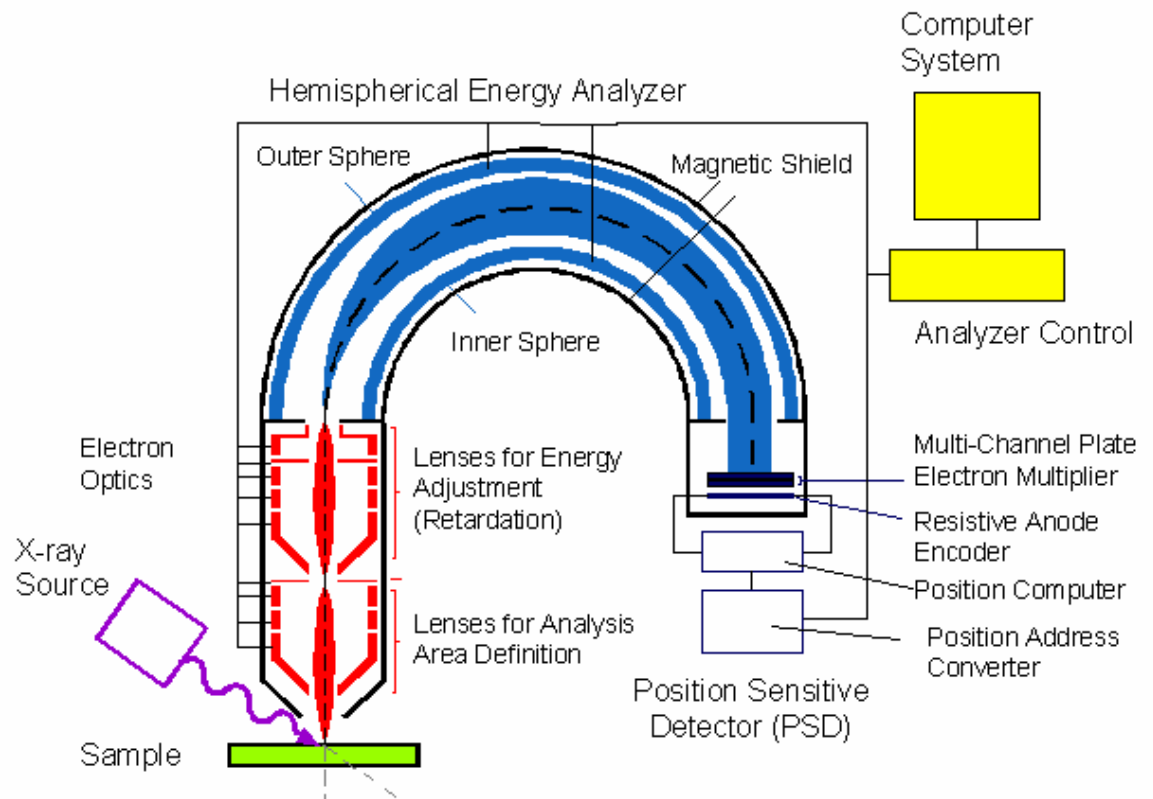


Figure 3-6: Schematics of XPS analyzer.²²

XPS is a very involved system, where the emitted electron encounters many interactions. XPS technique explores only a few nanometers of the sample, about 15 nm, for surface analysis, although the x-rays penetrate deep inside the sample. The multitude of the interactions that is experienced by the photoelectron limits the depths at which analysis can be done. Probability of the distance that can be traveled by a photoelectron without encountering inelastic scattering is given by

$$P(x) = ke^{\frac{-x}{\lambda}} \quad (3.7)$$

This technique also provides information of chemical composition; and identifies the oxidation states of ions. Therefore, XPS can be used to calculate different oxide thickness from the difference in escape probability, attenuation length, of the oxide²².

Since this system measures difference in binding energy, eq. 3.6, 1 eV resolution is an important parameter. This resolution is seen in the peak broadening and is comprised of the broadening from choice of X-ray, width of the analyzer energy window which is due to the physical setting of the detector, and the natural line width of the atomic orbital²². Adjustment of this resolution is limited since out of the three parameters listed here only the broadening from the physical setting of the detector can be adjusted once the X-ray source is set. This parameter usually offers a tradeoff between higher resolution and lower intensity, by changing the noise to signal ratio. Noise to signal ratio can be adjusted by changing the parameter of the lens mentioned above. Monochromatic and synchrotron sources, which have FWHM of 0.3-0.4 eV could be used in the place of the Al K α source used in this which has a FWHM of 0.85 eV to increase the resolution of the XPS spectrum collected here.

3.5 Physical Property Measurement System

Physical Property Measurement System (PPMS) was used to investigate the magnetic properties of the nanoparticles. The powdered samples were pressed and placed on a Kapton® tape, which was enclosed inside a plastic straw before mounting onto the PPMS dc extraction magnetometer. The magnetic measurements were performed by a dc magnetization measurements sequence. The dc measurements of the samples are performed by first cooling the system from room temperature to 5K in a zero magnetic field. At 5K, a 100 Oe magnetic field is applied and the magnetic moment was measured as the temperature was raised to room temperature at a rate of 1°C per minute. Measurements of the samples were repeated by maintaining the field as the samples cooled down to 5K, and the moment recorded as the temperature was raised to room temperature. These measurements are referred to as the Zero Field Cooled (ZFC), the former, and Field Cooled (FC), the later. Following these two magnetic measurements, moment versus field (hysteresis) as a function of temperature was also done up to 9 T. The hysteresis loops were taken at different temperature.

In PPMS measurements, voltage readings from the vibration of the samples inside the system with detection coils in response to a constant frequency and amplitude produced by the system were converted to magnetic flux readings. The vibrations of the samples near the sensing coils generate electromotive forces, which are translated into magnetizing forces. Samples with known values of correlation between magnetic flux and voltage reading are used to calibrate the system before measurement. This is derived from Faradays' law, which state that time rate of change of magnetic flux is equal to the electromotive force (emf) induced in a circuit²².

$$emf = -\frac{d\phi_B}{dt} = -A\frac{dB_{\perp}}{dt} \quad 3.7$$

Where B_{\perp} is the component of the magnetic field perpendicular to the loop and A is the area of a loop wire.

Chapter 4

RESULTS AND DISCUSSION

The crystal structure and phase composition present in the prepared sample, manganese oxide (Mn-O), is investigated by XRD, with a typical pattern from the study shown in Figure 4-1: X-ray diffraction pattern of the Mn-O core/shell nanoparticles.. The XRD patterns ranges from a 2θ angle of 30° to 90° , with a constant scan rate of $1.2^\circ/\text{min}$ and a step size of 0.02° , and revealed that the powdered sample has a polycrystalline nature. Although the pattern largely represents a disordered phase, the shallow peaks correspond to the major peaks of MnO, Mn₂O₃ and Mn₃O₄ according to JCPDS card number 75-0257, 76-0150, and 80-0382, respectively. None of the major peaks of MnO₂ corresponds to any of the collected pattern, JCPDS 81-2261 (see appendix of marked peaks). However the lack of well-defined peaks and inconsistency of peak ratio leaves any conclusion questionable, based solely on the nature of the pattern. Figure 4-2 (a-d), shows the HRTEM images of the powdered sample at different magnifications. The core/shell structure is confirmed from the image contrast on the HRTEM. This is expected for metallic NPs from the IGC after surface passivation. The particle size ranged from 15 to 25 nm. The presence of crystal planes both in the core and in the shell of the system confirms that the sample is not amorphous, however, their size indicates a polymorph system, which confirms the lack of well-defined peaks in the XRD pattern. Figure 4-2-a shows chains of nanoparticles agglomerated over a few hundred nanometers. The distinct core and the shell together form a composite with possible states of AFM core surrounded by a FiM shell, or FiM core surrounded by an

AFM shell which gives rise to EB magnetic interactions in this kind of core/shell structures. While the bulk of the core and shell remains unaffected and maintain their intrinsic magnetic phases, it is the spins close to the interface of the core and the shell that show exchange coupling as a result of spin canting, and spin-orbit-lattice coupling.

The nanoscale MnO particles are FM as revealed from the HRTEM and magnetometric measurements, comparable to those reported by Ortega et al.⁶⁷, while its bulk counterpart is AFM. The possible reason for this is in a bulk AFM the magnetic spins alternate forming two different kinds of sub-lattices and makes the net moment zero. However, in the nanostructured form each particle is isolated from its neighbor. In this circumstance the magnetic spins near the surface of each particle interact with the spins of their neighbors and couple themselves ferromagnetically if the inter-particle distance becomes comparable to the size of the particles themselves. However, in a diluted system they exhibit spin-glass type behavior instead.

The nanoscale MnO particles are FM as revealed from different experimental measurements, contrary to bulk MnO, which is AFM. A possible reason for this is that in a bulk AFM the magnetic spins alternate forming two different kinds of sub-lattices, making the net moment zero. However, in the nanostructured form, each particle is isolated from its neighbor and the uncompensated spins near the surface of each particle interact with the uncompensated spins of its neighbors. These spins couple ferromagnetically if the inter-particle distance becomes comparable to the size of the particles themselves. However, in a diluted system they exhibit spin-glass type behavior through the Ruderman-Kittel-Kasuya-Yosida (RKKY) type interaction.

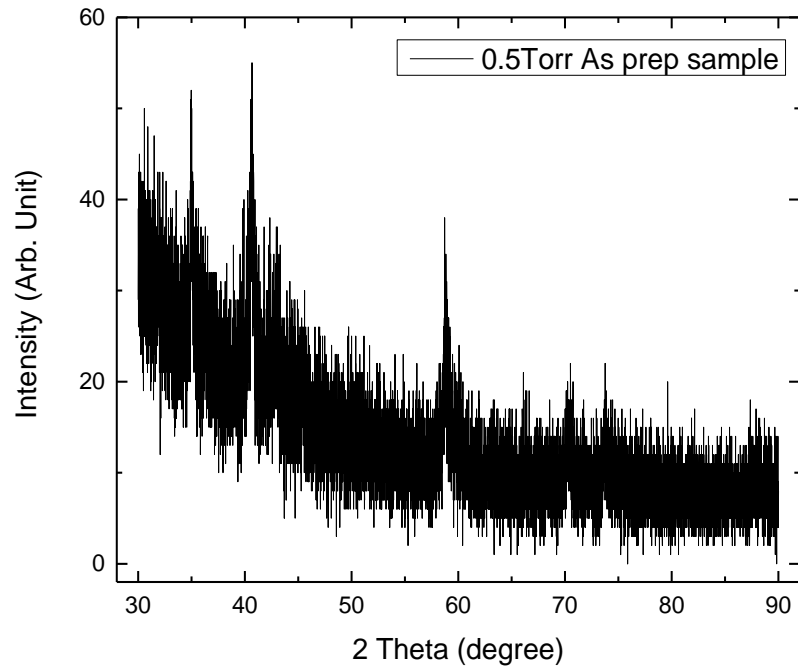


Figure 4-1: X-ray diffraction pattern of the Mn-O core/shell nanoparticles.

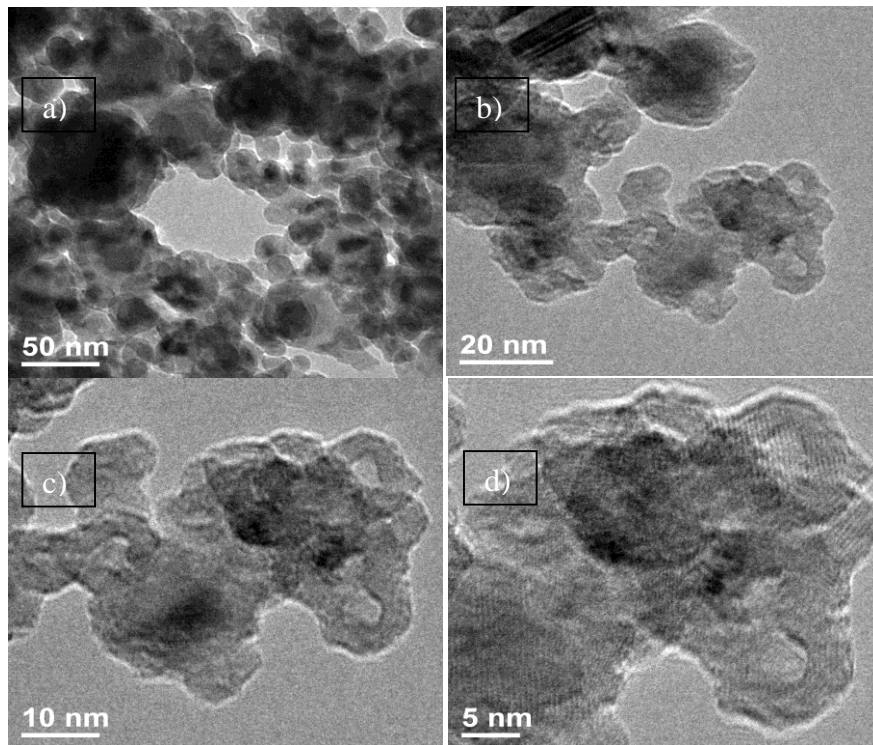


Figure 4-2: High resolution transmission electron microscopy image of the Mn-O core shell nanoparticles at different scale: a) 50 nm, b) 20 nm, c) 10 nm, and d) 5nm.

Figure 4-3 shows the X-ray photoelectron spectrum of Mn-O core/shell NPs. The obtained spectrum from the XPS system was corrected for charging on sample by comparing the initial and final carbon peaks scan which were conducted at the beginning and end of the Mn-O peaks scan, respectively. This corrected spectrum is very similar to that reported by Bonki et al.⁹⁸, and supports the existence of an oxide shell, however a distinction between MnO, Mn₂O₃, and Mn₃O₄ can't be made. Ortega et.al have shown that γ - Mn₂O₃ can also be formed as a result of MnO passivation. In our case we also claim formation of γ - Mn₃O₄ through passivation of MnO. A detailed analysis of the HRTEM images also suggests varying core sizes from as small as 5-6 nm to 15- 20 nm. These cores are irregular in shapes and appear to be multi-faceted. Nesbitt and Banerjee discussed in detail the difficulties in using XPS spectra to identify different oxide states of manganese (Mn²⁺, Mn³⁺, and Mn⁴⁺)⁹⁹. The XPS spectrum of manganese oxide leads to a very broad peak, which is due to the high spin nature of the oxides⁹⁹. The difference in binding energy of the different oxide states is within 2 eV, making a clear distinction between these binding energies very difficult; especially since most XPS system have a system FWHM around 1 eV. This study confirms what we already knew from the XRD pattern and the HRTEM image: we have multi-oxide system. Our XPS result shows small peaks around the principal peak. These less intense peaks fall within an energy band of 2 eV. We assume that these peaks represent all possible ionic states Mn²⁺, Mn³⁺, Mn⁴⁺. Since our XPS system resolution limits exact identification of the ionic states within an energy difference of 2 eV, it is difficult to pinpoint which ionic states of manganese are present.

The HRTEM images also reveal some un-oxidized nanoparticles which are assumed to be metallic Mn. These metallic particles are possibly formed due to rapid coalescence of Mn atoms clustering with each other in oxygen deficient regions, forming

agglomerated clusters of Mn NPs. While these regions were observed, most of the sample was Mn/Mn-O core/shell nanoparticles.

Within the clusters of Mn-O nanoparticles, the particles maintain inter-granular boundaries making it a multi-granular MnO region. Some of the cores are observed to be agglomerated clusters of Mn with either Mn_3O_4 or Mn_2O_3 shells or vice-versa. It was shown earlier that structure of the passivation shell in core/shell Mn-O NPs depends on the shell size being primarily $\gamma\text{-Mn}_2\text{O}_3$ for small cores and progressively transforming to Mn_3O_4 for larger cores. Based on this statement we infer that the smaller size shell as seen in the HRTEM images is $\gamma\text{-Mn}_2\text{O}_3$ while the relatively larger size particles are Mn_3O_4 . Thus we claim that we have in our fabricated samples an assembly of mixed FM and AFM shell. In addition the HRTEM also suggest the presence of some hollow nanoparticles of Mn-O. Kwangjin An, et al. have reported synthesizing various hollow oxide nanoparticles from as-prepared Mn-O and iron oxide NPs with partially amorphous surface with surface energy¹⁰⁴. Kwangjin An et al. also report that MnO NPs are weakly FM at low temperature while it is AFM in bulk form at the same temperature regime. The magnetic moment of MnO nanocrystals comes from Mn^{2+} ions at the partially amorphous surface. As a result, the magnetic property of the amorphous nanoparticles containing Mn^{2+} ions would be similar to that of MnO nanocrystals. This is in complete contrast with iron oxide (Fe_3O_4) nanocrystals which maintain their ferromagnetic nature because the magnetic moments of Fe^{3+} are stabilized by the crystal symmetry. Thus we observed in our sample some kind of unconventional EB effect as revealed from the magnetization measurements at different temperatures in the low temperature regime.

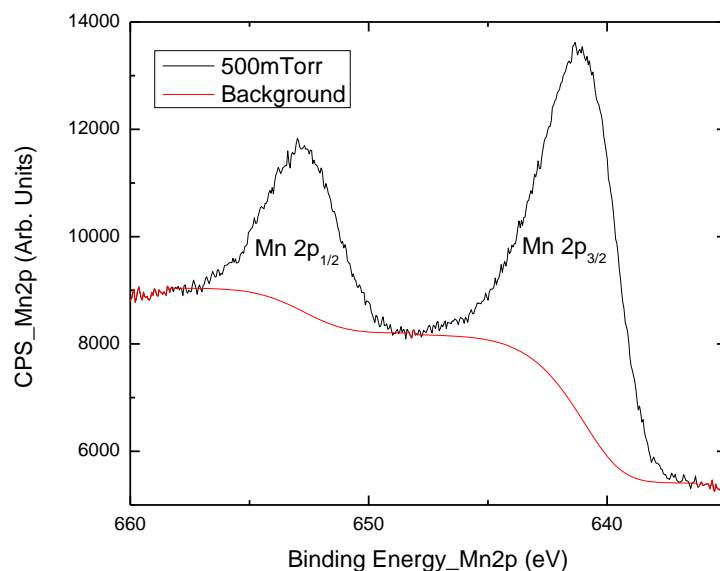


Figure 4-3: X-ray photoelectron spectrum of the Mn-O core/shell nanoparticles.

Of the stable oxide states of manganese, MnO and MnO₂ are AFM with a T_N of 143K for and 92K, respectively. However, Wang et al. have shown increases in T_N as particles size decreases¹⁰¹. Mn₂O₃ and Mn₃O₄ have T_C's both around 43K, more specifically 39K and 42K, respectively⁶⁷, although the nature of the size change is not as well discussed in the T_C regime. The magnetic behavior of the sample as a function of temperature is shown in Figure 4-4: FC and ZFC curves of Mn-O core/shell nanoparticles from 5K to 300K with inset from 5k to 72K, where both the ZFC and FC measurements are shown. The behavior revealed here is in agreement with results presented by Ortega et al.⁶⁷ where particles of similar sizes exhibit the same behavior. Figure 4-4: FC and ZFC curves of Mn-O core/shell nanoparticles from 5K to 300K with inset from 5k to 72K also shows the characteristic temperature of the system, with the flip and blocking temperature (T_f) and (T_B) at 42K and T_C at approximately 47K, which is slightly higher than the reported value for both of the bulk materials. The T_N is well above 150K, which shows that AFM nature of the MnO core persists well above the

reported T_N of the bulk MnO. The FC and ZFC curves exhibit a typical Néel relaxation behavior of the magnetic moments. Moment relaxation strongly depends on the size distribution of the particles. From the nature of the ZFC curve we ascertain that the fabricated MnO particles have a relatively narrow size distribution and the average spin flip time is on the order of 10^{-8} sec for the particle size distribution of 10-50 nm. The spin flip time is shorter for smaller particles.

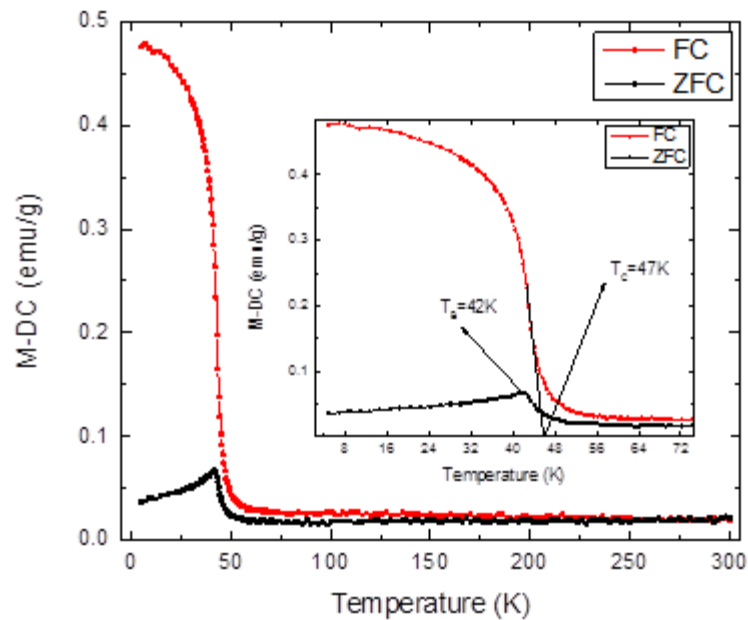


Figure 4-4: FC and ZFC curves of Mn-O core/shell nanoparticles from 5K to 300K with inset from 5k to 72K.

Figure 4-5: Hysteresis loops of the Mn-O core/shell nanoparticles from 5K to 42K. shows the hysteresis loop of Mn-O core/shell NPs from 5K to 42K. Two interesting observations can be made from this figure. One is the pinching nature of the loop at low field around the T_B (42K), and the second is the increase in H_{EB} the T_N . The constriction and broadening of the hysteresis curve at T_B bears the signature of a springy magnetic interaction among different size particles, where different magnetic behaviors are

observed for different particle sizes. Loop broadening indicates a good correlation between the domain size and size of the particle. When the particles become a single magnetic domain and the size of the particles are equal to the domain size, the effect is depicted by a loop broadening which means a higher coercivity. This is the most desirable condition for high density recording devices. We believe that the particles have achieved that limit. Subsequent narrowing down (constriction) at relatively lower field indicates a soft magnetic behavior of the particles. Thus we conclude that there is an ensemble of particles in our system. One class of particles behaves as soft while the other as hard magnetic particles. Presence of soft and hard magnetic entities in the same matrix would depict a “spring exchange type behavior”. We claim that our studied material has such behavior. Figure 4-7: Exchange bias field of the Mn-O nanoparticles from 5K to 300K further shows this trend, it shows multiple transitions around the reported T_B and also an increase in the shift as the temperature rises from 150K up to room temperature. The saturation magnetization is observed to sharply decrease from a very high value of 10.67 emu/g at 5K down to 5.18 emu/g at 65K then decrease slowly until room temperature to a value of 2.78 emu/g.

Figure 4-6: Magnetic coercivity of the Mn-O core/shell nanoparticles from 5K to 300K shows the coercivity of the sample to decrease with an increase in temperature. This trend is comparable to the reported values for a similar system discussed by Ortega et al⁶⁷. The high coercivity, a little over 20 kOe, of the material is attributed to the large anisotropy of the Mn_2O_3 and Mn_3O_4 , and the canting effect expected between Mn^{+2} and Mn^{+3} or Mn^{+4} . The sharp decrease of the coercivity as a function of temperature is expected. However, the sample never reaches zero coercivity, and this can be attributed to the strong interaction between the AFM core and FiM shell that persist well above the T_N of the sample.

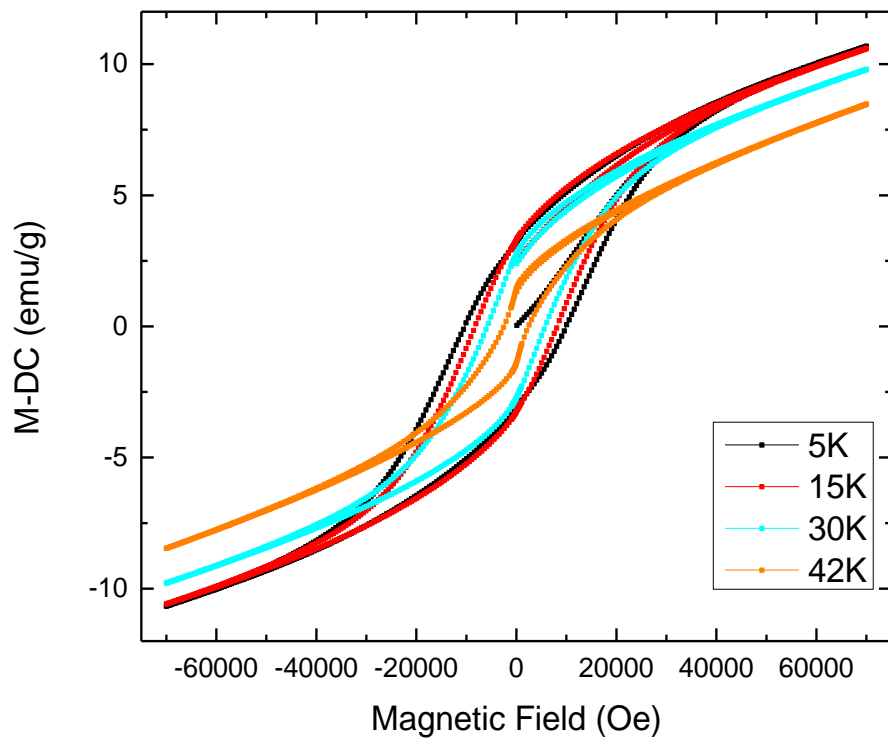


Figure 4-5: Hysteresis loops of the Mn-O core/shell nanoparticles from 5K to 42K.

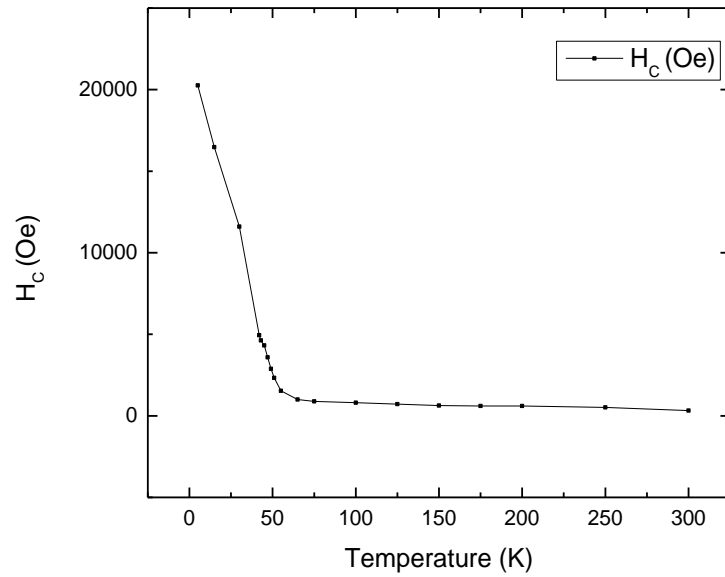


Figure 4-6: Magnetic coercivity of the Mn-O core/shell nanoparticles from 5K to 300K.

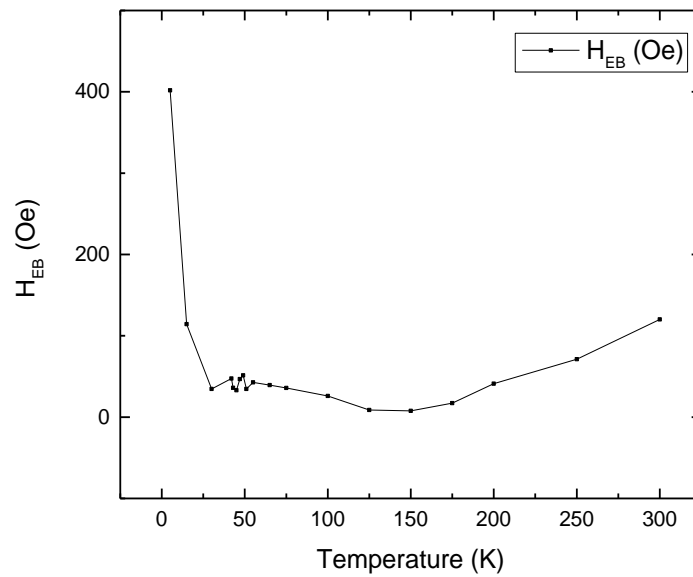


Figure 4-7: Exchange bias field of the Mn-O nanoparticles from 5K to 300K.

Chapter 5

CONCLUSION

Core/shell Mn-O magnetic NPs have been successfully fabricated by IGC technique. The crystal structure and phase composition of the prepared sample were investigated by XRD, XPS, and HRTEM. The identifiable peaks from the XRD pattern suggested the presence of MnO, Mn₂O₃, and Mn₃O₄. The nature of the XRD pattern made it difficult to make a clear distinction between the different phases. HRTEM confirmed the core/shell structure and particle size of the prepared sample, which ranged from 15 to 25 nm. The particles form random clusters and agglomerates. HRTEM also shows the polymorph nature of the prepared samples. Magnetic analysis suggests an antiferromagnetic (AFM) core surrounded by a ferrimagnetic (FiM) shell. A significant H_{EB} has been observed between the core and shell in the temperature regime of $T < T_C < T_N$, where T_N is the Néel temperature of the AFM core and T_C is the FiM Curie temperature of the shell. The magnetic properties are investigated through measurements of the magnetic isotherms at different temperatures. The shift in the hysteresis loop (H_{EB}) is observed to be maximum at 5K, the lowest temperature recorded, with $H_{EB}=200$ Oe. The H_{EB} is observed to be maximum at 5K, with a coercivity field (H_C) =20.25 kOe. The temperature profile of H_{EB} shows three distinct regions: first, the decrease of the change in shift up to the $T_B = 42$ K, second, a sudden increase then decrease, third, an increase from around 150K to room temperature, the highest temperature recorded. H_{EB} is attributed to the spin canting and fluctuating ionic interaction between the Mn⁺² and Mn⁺³ states, which are strongest near the boundary of the core and shell. FC and ZFC dc magnetization suggest super para-magnetism, accompanied by magnetic hysteresis below

T_B . T_B decreases with the increase in particle size. The relatively sharp transition in the ZFC curve indicates a narrow particle size distribution.

Through this research work an attempt has been made to fabricate core/shell structure NPs of Mn-O with different oxides of manganese and to investigate the interaction between the core and shell. It's observed that the H_{EB} is not a typical phenomenon in only layered and ordered structures. This effect is also prominent in NPs of different magnetic elements. The XPS study has revealed the oxidation states of Mn-O in general. However instrumental limitation on finer resolution of different ionic states of Mn has made it difficult to accurately identify the Mn^{2+} , Mn^{3+} , and Mn^{4+} ionic states of Mn. Based on HRTEM images and the magnetic studies on the fabricated samples we assume that three oxidation states on Mn are present in the as made core/shell nanoparticle samples. We also believe that the as made sample is composed of a mixed core/shell and inverted core/shell structures of Mn-O. It is anticipated that much more interesting transport properties can be revealed through careful investigation of the ac and dc electrical and magnetic properties of this type of core/shell structured Mn-O. The impedance and dielectric behavior of this material can be a very good addition to the properties already known. A thorough study of the dissipation factors and identification of the frequency range for maximum absorption of electromagnetic radiation may also add new dimension to the complete picture of Mn-O core/shell NPs.

REFERENCES

1. W. Levason and C. A. McAuliffe, *Coord. Chem. Rev.*, 7, 353 (1972).
2. A. R. Armstrong, P. G. Bruce, *Nature*, 381, 499-500 (1996).
3. W. S. Seo, H. H. Jo, K. Lee, B. Kim, S. J. Oh, J. T. Park, *Angew. Chem., Int. Ed.*, 43, 1115-1117 (2004).
4. M. Anilkumar, V. Ravi, *Mater. Res. Bull.*, 40, 605-609 (2005).
5. Y. F. Shen, R. P. Zerger, R. N. DeGuzman, S. L. Suib, L. McCurdy, D. I. Potter, C. L. O'Young, *Science*, 260, 511-515 (1993).
6. M. E. McHenry and D. E. Laughlin, *Acta Mater.*, 48, 223 (2000).
7. H. Gleiter, *Acta Mater.*, 48, 1 (2000).
8. H. Gleiter, *Prog. Mater. Sci.*, 33, 223 (1989).
9. T. Ahmad, K. V. Ramanujachary, S. E. Loflan, and A. K. Ganguli, *J. Mater. Chem.*, 14, 3406-3410 (2004).
10. S. Wei, Q. Wang, J. Zhu, L. Sun, H. Lin, and Z. Guo, *Nanoscale*, 3, 4474 (2011).
11. C. B. Murray, S. H. Sun, W. Gaschler, H. Doyler, T. A. Betley and C. R. Kagan, *IBM J. Res. Dev.*, 45, 47 (2001).
12. F. Fettar, S. F. Lee, F. Petroff, A. Vaures, P. Holody, L. F. Schelp and A. Fert, *Phys. Rev. B: Cond. Matter Mater. Phys.*, 65, 174415 (2002).
13. B. M. Berkovsky, V. F. Medvedev and M. S. Krakow, *Magnetic Fluids: Engineering Applications*, Oxford University Press, Oxford, 1993.
14. S. P. Gubin, Y. I. Spichkin, Y. A. Koksharov, G. Y. Yurkov, A. V. Kozinkin, T. I. Nedoseikina, M. S. Korobov and A. M. Tishin, *J. Magn. Magn. Mater.*, 265, 234 (2003).
15. V. F. Puentes, P. Gorostiza, D. M. Aruguete, N. G. Bastus and A. P. Alivisatos, *Nat. Mater.*, 3, 263 (2004).
16. K. V. P. M. Shafi, A. Gedanken and R. Prozorov, *Adv. Mater.*, 10, 590 (1998).

17. M. P. Pileni, *Adv. Funct. Mater.*, 11, 323 (2001).
18. G. X. Chen, M. H. Hong, B. Lan, Z. B. Wang, Y. F. Lu and T. C. Chong, *Appl. Surf. Sci.*, 228, 169 (2004).
19. J. E. Post, *Biominalisation Processes of Iron and Manganese*, Calena Supplement 21, N. C. W. Skinner and R.W. Fitzpatrick, ed., Catena Verlag, Reiskirchen, Germany, pp. 51-73, (1992).
20. R. Tsybukh, *A Comparative Study of Platinum Nanodeposits on HOPG (0001), MnO(100) and MnO_x/MnO(100) Surfaces by STM and AFM after Heat Treatment in UHV, O₂, CO and H₂*. Leiden: Leiden Institute of Chemistry, CASC Faculty of Science, Leiden University, 2010. Print.
21. A. Ceylan, *Core/Shell structured Magnetic Nanoparticles Synthesized by Inert Gas Condensation*, Newark: University of Delaware, Faculty of the University of Delaware, 2007. Print.
22. G. H. Jaffari; *Morphological, magnetic and electronic structural studies of nanostructured spinel ferrites*, Newark: University of Delaware, Faculty of the University of Delaware, 2012. Print.
23. A. F. Wells, *Structural Inorganic Chemistry*, 5th ed., (Oxford University Press, Oxford, UK, 1984).
24. N. N. Greenwood, A. Earnshaw, (1997). *Chemistry of the Elements* (2nd Ed.). Butterworth–Heinemann.
25. I. L. Knunyants, *Khimicheskaya entsyklopedia*, Vol. 2, (The Publishing House Sovetskaya entsyklopediya, Moskow, 1990) [in Russian].
26. R. T. Downs, M. Hall-Wallace, *Am. Mineral.* 88, 247-250 (2003).
27. C. Picard, P. Gerdanian, *J. Sol. State Chem.* 11, 190-202 (1974).
28. A. Agopsowicz, J. L. Hitchcock, F. L. Tye, *Thermochimica Acta* 32, 63-71 (1979).
29. D. J. Morgan, A. E. Milodowski, S. St. J. Warne, S. B. Warrington, *Thermochimica Acta* 135, 273-277 (1988).
30. F. Tedjar, J. Guitton, *Thermochimica Acta* 181, 13-22 (1991).

31. S. Fritsch, A. Navrotsky, *J. Am. Ceram. Soc.* 79 (7), 1761-1768 (1996).
32. C. Gonzalez, J. I. Gutiérrez, J. R. González-Velasco, A. Cid, A. Arranz, J. F. Arranz, *J. Therm. Anal.* 47, 93-102 (1996).
33. S. Fritsch, J. E. Post, A. Navrotsky, *Geochim. Cosmochim. Acta* 61, 2613-2616 (1997).
34. M. I. Zaki, M. A. Hasan, L. Pasupulety, K. Kumari, *Thermochimica Acta* 311, 97-103 (1998).
35. S. Fritsch, J. Sarrias, A. Rousset, G. U. Kulkarni, *Mater. Res. Bull.* 33 (8), 1185-1194 (1998).
36. C. B. Azzoni, M. C. Mozzati, P. Galinetto, A. Paleari, V. Massarotti, D. Capsoni, M. Bini, *Solid State Comm.* 112, 375-378 (1999).
37. B. Gillot, M. El Guendouzi, M. Laarj, *Mater. Chem. Phys.* 70, 54-60 (2001).
38. Q. Zhao, W.-H. Shih, *Microp. Mesop. Mat.* 53, 81-86 (2002).
39. V. B. Fetisov, A. V. Fetisov, N. V. Korchemkina, L. A. Ovchinnikova, E. A. Pastukhov, and A. Ya. Fishman, *Dokl. Phys. Chem.* 387, 291-293 (2002).
40. K. M. Parida, S. B. Kanungo, *Thermochimica Acta* 66, 275-287 (1983).
41. T. Ahmad, K. V. Ramanujachary, S. E. Lofland and A. K. Ganguli, *J. Mater. Chem.* 14, 3406-3410 (2004).
42. J. Park, K. An, Y. Hwang, J.-G. Park, H.-J. Noh, J.-Y. Kim, *Nat. Mater.* 3, 891-895 (2004).
43. H. Yi-Fan, C. Fengxi, Z. Z. Yi, K. Ramesh, C. L. Wei, E. Widjaja, *J. Phys. Chem. B* 110 (48), 24450-24456 (2006).
44. Z. Wu, K. Yu, Y. Huang, C. Pan, Y. Xie, *Chemistry Central Journal* 1:8, 1-9 (2007). <http://journal.chemistrycentral.com/content/1/1/8>.
45. Y. Chen, E. Johnson, X. Peng, *J. Am. Chem. Soc.* 129 (35), 10937-10947 (2007).
46. M. Salavati-Niasaria, F. Davar, M. Mazaheric, *Polyhedron* 27 (17), 3467-3471 (2008).

47. W. Kalisvaart, R. Niessen, P. Notten, Electrochemical hydrogen storage in mgsc alloys: a comparative study between thin films and bulk materials, *J. Alloys Comp.* In Press, Corrected Proof, Available online 9 November 2005.
48. Y. Chabre, J. Pannetier, *Prog. Solid St. Chem.* 23, 1-130 (1997).
49. J. E. Post, *Natl. Acad. Sci. USA* 96, 3447-3454 (1999).
50. A. H. Pfund, *Phys. Rev.*, 35, 1434 (1930).
51. R. Birringer and H. Gleiter, *Phys. Lett.*, 102A, 365 (1984).
52. H. Gleiter, *Progress in Matter. Sci.*, 33, 223 (1989).
53. C. G. Granqvist and R. A. Buhrman, *J. Appl. Phys.*, 47, 2200 (1976).
54. A. R. Tholen, *Acta Metalurgica*, 27, 1765 (1979)
55. S. Yatsuya, S. Kasukabe, and R. Uyeda, *Jpn. J. Appl. Phys.*, 12, 1675 (1973).
56. R. B. a. R. F. C. M B Ward, *J. Phys.: Conf. Ser.* 26 296 (2006).
57. T. Ahmad, K. V. Ramanujachary, S. E. Loftland, and A.K. Ganguli, *J. Mater. Chem.*, 2004, 14, 3406-3410.
58. M. Baldi, E. Finocchio, F. Milella and G. Busca, *Appl. Catal.. B*, 16, 43 (1998).
59. M. F. M. Zwinkels, S. G. Jaras, P. G. Menon and T. A. Griffik, *Catal. Rev. Sci. Eng.*, 35, 319 (1993).
60. M. Baldi, *Appl. Catal.*, B, 17, L175 (1998).
61. H. M. Zhang and Y. Teraoka, *Catal. Today*, 6, 155 (1989).
62. Y. F. Chang and J. G. McCarty, *Catal. Today*, 30, 163 (1996).
63. G. H. Lee, S. H. Huh, J. W. Jeong, B. J. Choi, S. K. Kim and H. C. Ri, *J. Am. Chem. Soc.*, 124, 12094 (2002).
64. C. N. R. Rao and G. V. Subba Rao, *Phys. Status Solidi A*, 1, 597 (1970).

65. A.E. Berkowitz, G. F. Rodriguez, J. I. Hong, K. An, T. Hyeon, N. Agarwal, D. J. Smith, and E. E. Fullerton, *Phys. Rev. B*, 77, 02443 (2008)).
66. V. Golosovdky, G. Salazar-Alvarez, A. Lopez-Ortega, M. A. Gonzalez, J. Sort, M. Estrader, S. Surinach, M. D. Baro, and J. Nogues, *Phys. Rev. Lett.*, 102, 247201 (2009).
67. A. Lopez-Ortega, D. Tobia, E., Winkler, I. V. Golosovsky, G. Salazar-Alvarez, S. Extrade, M. Estrader, J., Sort, M. A. Gonzalez, S. Surinach, J. Arbiol, Francesca Peiro, R. D. Zysler, M. D. Baro, J. Nogues. *J. Am. Chem. Soc.* , 132, 9398 (2010).
68. B. Boucher, R. Buhl and M. Perrin, *J. Appl. Phys.*, 42, 1615 (1971).
69. K. Dwight and N. Menyuk, *Phys. Rev.*, 119, 1470 (1960).
70. A. Ceylan, A. K. Rumaiz, S. I. Shah, *J. of Applied Physics*, 101, 094302 (2007).
71. A. Ceylan, C. Baker, and I Shah, *J. of Applied Physics*, 100, 034301 (2006).
72. G. H. Jaffari, S. R. Ali, S. K. Hasanain, G. Guntherodt, and S. I. Shah, *J. of Applied Physics*, 108, 063921(2010).
73. B. D. Cullity, *Introduction to Magnetic Materials; Vol.2*, edited by Wiley-IEEE Press 2nd edition, 2008. Print
74. W. H. Meiklejohn and C. P. Bean, *Phys. Rev.*, 102, 1413 (2956).
75. R.W. Chantrell, M. El-Hilo, and K. O'Grady, *IEEE Trans. Magn.*, 27, 3570 (1991).
76. J. Keller, P. Miltenyi, B. Beschoten, G. Guntherodt, U. Nowak, and K. D.Usadel, *Phys. Rev. B.*, 66, 014431 (2002)
77. J. Noguès, C. Leighton, and Ivan .K. Shuller, *Phys. Rev. B.*, 61, 1315 (2000).
78. M. Kiwi, J. Mejia-Lopez, R. D. Portugal and R. Ramirez, *Europhys. Lett.*, 48, 573 (1999).
79. M. Kiwi, J. Mejia-Lopez, R. D. Portugal and R. Ramirez, *Appl. Phys. Lett.*, 75, 3995 (1999).
80. U. Nowak, K. D. Usadel, J. Keller, P. Miltenyi, B. Beschoten, and G. Guntherodt, *Phys. Rev. B.*, 66, 014430 (2002).

81. L. Nèel, J. Ann. Phys. Paris 2, 61 (1967).
82. A. P. Malozemoff, Phys. Rev. B. 35, 3679 (1987).
83. P. Zaag, A. R. Ball, L. F. Feiner, R. M. Wolf, and P. Heijden, J. Appl. Phys., 79, 5103 (1996).
84. S. Soeya, S. Nakamura, T. Iamgawa, and S. Narishiye, J. Appl. Phys., 77, 5838 (1995).
85. K. Hoshino, S. Noguchi, R. Nakatani, H. Hoshiya, and Y. Siguta, Jpn. J. Appl. Phys., 33, 1327 (1994).
86. T. Ambrose and C. L. Chien, J. Appl. Phys., 83, 6822 (1998).
87. A. J. Devasahayam and M. H. Kryder, J. Appl. Phys., 85, 5519 (1999).
88. A. Hoffmann, Phys. Rev. Lett., 93, 097203 (2004).
89. R. Delhez, Th. Keijser and E. Mittemeijer, J. Phys. E. Sci. Instrum., 11, 649 (1978).
90. B. David, Transmission Electron Microscopy: a textbook for material science, 2nd ed., Springer, 2009. Print
91. A. Aharoni, Introduction to the Theory of Ferromagnetism, Oxford University Press, 2nd edition, p.105-108 (2000).
92. H. Z. a. S. D. Bader, Magnetic Heterostructures; 1st ed., Springer, 2007. Print
93. J. Nogues and I. K. Schuller, Journal of Magnetism and Magnetic Materials, 192, 203 (1999).
94. R. E. Fontana, S. A. MacDonald, H. A. A. Santini, and C. Tsang, IEEE Trans. Magn., 35, 806 (1999).
95. X. Batlle, A. Labarta, J. Phys. D: Appl. Phys., 35, R15 (2002).
96. C. L. Chien, Annu. Rev. Mater. Sci., 25, 129 (1995).
97. R. Skomski, J. Phys. D: Condens. Matter., 15, R841 (2003).

98. J. F. Bonki, D. D. Oyler, X. Ke, P. Schiffer, R. E. Schaak, *J. Am. Chem. Soc.*, 131, 9145(2009).
99. H.W. Nesbitt and D. Banerjee, *American Mineralogist*, 83, 305-315(1998).
100. P. Martin, *Evaporation: Processes, Bulk Microstructures and Mechanical Properties*, in *Handbook of Thin Films*, edited by Wiley, New York, 2009. Print
101. X. Wang and Y. Li, *Chem. Eur. J*, 9, 1(2003).
102. N. Winograd, S. W. Gaarenstroom, *Physical Methods in Modern Chemical Analysis*, 2, 115-169(1980).
103. S. Shanmugam, A. Gedanken, *J. Phys. Chem. B*, 110, 48(2006).
104. A. Kwangjin, H, Taeghwan, *Nano Today*, 4, 359-373(2009).

Appendix

SUPPLEMENTAL FIGURE

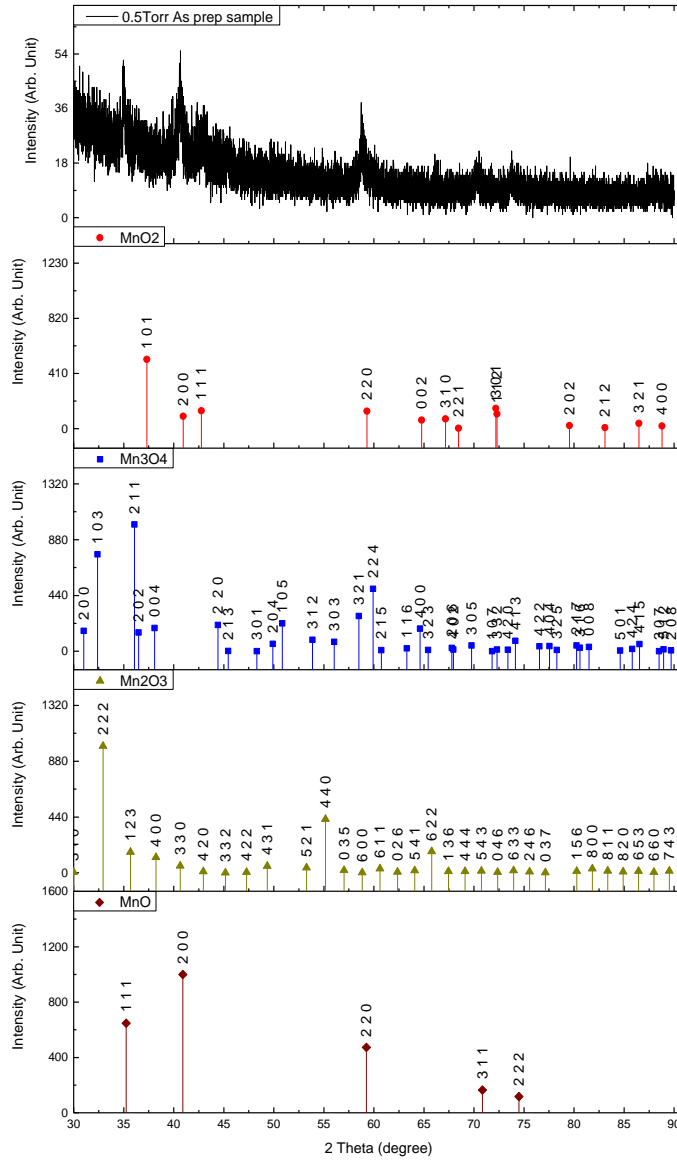


Figure A-1: XRD pattern with JCPDS data of MnO, Mn₂O₃, and Mn₃O₄.